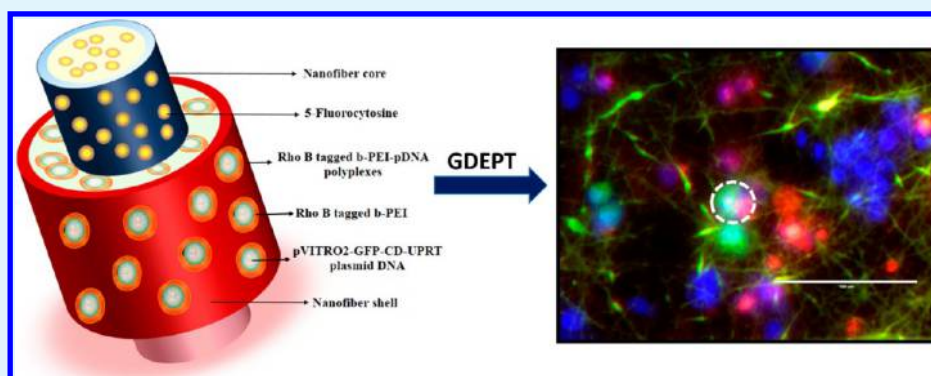


Bioactive Core–Shell Nanofiber Hybrid Scaffold for Efficient Suicide Gene Transfection and Subsequent Time Resolved Delivery of Prodrug for Anticancer Therapy

Uday Kumar Sukumar[†] and Gopinath Packirisamy^{*,†,‡}

[†]Nanobiotechnology Laboratory, Centre for Nanotechnology, [‡]Department of Biotechnology, Indian Institute of Technology Roorkee, Roorkee, Uttarakhand-247667, India

S Supporting Information



ABSTRACT: Nanofiber scaffold's ability to foster seemingly nonexistent interface with the cells enables them to effectively deliver various bioactive molecules to cells in the vicinity. Among such bioactive molecules, therapeutically active nucleic acid has been the most common candidate. In spite of such magnanimous efforts in this field, it remains a paradox that suicide gene delivery by nanofibers has never been sought for anticancer application. To investigate such a possibility, in the present work, a composite core–shell nanofibrous scaffold has been realized which could efficiently transfect suicide gene into cancer cells and simultaneously deliver prodrug, 5-Fluorocytosine (5-FC) in a controlled and sustained manner. The scaffold's ability to instigate apoptosis by suicide gene therapy in nonsmall lung cancer cells (A549) was ascertained at both phenotypic and genotypic levels. A cascade of events starting from suicide gene polyplex release from nanofibers, transfection, and expression of cytosine deaminase-uracil phosphoribosyltransferase (CD::UPRT) suicide gene by A549; subsequent prodrug release; and its metabolic conversion into toxic intermediates which finally culminates in host cells apoptosis has been monitored in a time-dependent manner. This work opens up new application avenues for nanofiber-based scaffolds which can effectively manage cancer prognosis.

KEYWORDS: core–shell nanofibers, gene transfection, suicide gene, prodrug, anticancer therapy

1. INTRODUCTION

The ease of polymer nanofiber fabrication and versatility of electrospinning by itself has catered wide scope for developing nanofiber based multifaceted drug delivery systems. At present, these electrospun nanofibers have already witnessed unparalleled share of success in controlled and sustained delivery of diverse bioactive molecules (i.e., drugs, siRNA, DNA, proteins, and nanoparticles). In recent years, apart from drugs, nucleic acid delivery by nanofibers has also been pursued extensively for gene therapy applications.¹ Such nanofiber based gene therapy approach by virtue of being localized administration owns a clear edge over other polymer based gene delivery formulations in terms of therapeutic index. Moreover, the controlled release of therapeutic nucleic acids from nanofibers renders scope for higher and prolonged dosages which otherwise remains elusive, and thereby it also does not tend

to elicit systemic toxicity after administration. Apart from this, the extracellular matrix (ECM) look-alike morphology of nanofibers narrows the interface between the target cells and the therapeutic genes to be delivered.²

Although nanofiber based gene therapy has evolved its course for a decade, its use for suicide gene therapy (gene directed enzyme prodrug therapy (GDEPT)) has remained unexplored until now. The term “suicide gene therapy” by itself is readily comprehensible, which denotes delivery of gene encoding a functional enzyme which is not toxic per se but which potentiates the target cells to catalyze the conversion of therapeutically less active prodrug into highly toxic com-

Received: June 14, 2015

Accepted: August 3, 2015

Published: August 3, 2015

pounds.³ The toxic metabolic intermediates thereby generated certainly effectuate their therapeutic potential on the native cell and also tend to permeate into cells in the vicinity so as to mediate their bystander effects. Owing to such bystander effects, higher transfection efficiency does not remain a prerequisite anymore for complete eradication of tumors by suicide gene therapy. The use of suicide genes further confines the prodrug therapeutic potentials to the cells solely expressing appropriate enzyme (encoded by the suicide gene) which otherwise remain nontoxic unless otherwise acted upon by the enzymes.

A panoptic study of suicide gene strategies thus far has revealed various combinatorial enzyme-prodrug systems, of which thymidine kinase, cytosine deaminase, purine nucleoside phosphorylase (PNP) carboxypeptidase A1, and nitroreductase deserve mention owing to their significant success.⁴ The present work thrusts on therapeutic potential of genetically engineered dual-enzyme suicide gene, CD::UPRT, and prodrug 5-FC. The enzyme cytosine deaminase (CD) converts 5-FC to 5-Fluorouracil (5-FU), a catabolic inhibitor of thymidine synthetase enzyme which stalls nucleic acid synthesis and which also leads to miss-incorporation of bases (i.e., mutations) and thereby triggers a cascade of signaling pathways which finally culminates in cellular apoptosis. Owing to poor 5-FU stability and lack of bystander effects in CD/5-FC enzyme-prodrug system, it does not attain significant therapeutic outcomes. Therefore, to further supplement the therapeutic potential of CD/5-FC system, another enzyme uracil phosphoribosyl transferase (UPRT) in also inculcated, which converts 5-FU into cytotoxic 5-fluorouracilmonophosphate (5-FUMP) which is later catalyzed to even more toxic byproducts 5-fluorodeoxyuracilmonophosphate (5-FdUMP) and 5-fluorouraciltriphosphate (5-FUTP).⁵ Preexisting literature on targeted delivery of CD::UPRT suicide gene by means of mesenchymal stem cells further strengthens the therapeutic efficacy of the suicide gene (i.e., CD::UPRT) under study.^{6,7} Taking into consideration such improved therapeutic prospects of CD::UPRT/5-FC system, its anticancer potentials are put to test in this work.

Among the various nonviral transfecting agents, polycationic polyethylenimine has drawn huge attention owing to its ability to efficiently condense DNA to form stable polyplexes.⁸ Apart from this, branched polyethylenimine (bPEI) presence renders the polyplexes an ability to circumvent endosomal degradation by proton sponge effect and thereby delivers intact suicide gene to the cell cytoplasm.⁹ Thrusting upon such prenotions, bPEI and pVITRO2-GFP/CD::UPRT plasmid polyplexes were synthesized at different nitrogen/phosphate (N/P) ratios for asserting a trade-off between polyplexes stability and transfection efficiency, the most appropriate of which was then incorporated within the nanofibers by blend electrospinning.

Efficient suicide gene therapy begins with suicide gene transfection into the host cell which is subsequently followed by administration of prodrug. In coherence with a similar trend, the present work evaluates core-shell nanofibrous scaffold for delivery of suicide gene and prodrug. Presynthesized suicide gene-bPEI polyplexes are loaded in the nanofiber shell by virtue of which they are predominantly released during the initial phase of incubation, and they transfect the cells in the vicinity, followed by sustained release of prodrug (5-FC) loaded in the nanofiber core. As pVITRO2-GFP/CD::UPRT-bPEI polyplexes and 5-FC are localized in different layers of core-shell nanofibers (outer shell and inner core of nanofiber,

respectively), they follow a distinct release profile which is most appropriate for fostering anticancer potentials of suicide gene therapy. Differential cross-linking of nanofibers also extends the possibility of altering the polyplexes and prodrug release profile. Thus, this work envisions core-shell nanofibers as a versatile means of simultaneously delivering suicide gene and the prodrug in a controlled and sustained manner.

2. MATERIALS AND METHODS

Materials. Poly(ethylene oxide) (PEO) (M_v : 900 000) and branched poly(ethylenimine) (bPEI) (M_w : 25 000) were purchased from Sigma-Aldrich. Prodrug, 5-FC and fluorescent stains, propidium iodide (PI), and Hoechst 33342 were also procured from Sigma-Aldrich and were stored at appropriate temperature until used. *N*-(3-(dimethylamino)propyl)-*N'*-ethylcarbodiimide (EDC), *N*-hydroxysuccinimide (NHS), and cellulose dialysis membrane-132 (molecular weight cutoff (MWCO), 12 kDa) were acquired from HiMedia. Heparin sodium salt (extracted from bovine intestinal mucosa) and Deoxyribonuclease I (DNase I) (extracted from bovine pancreas) were purchased from SRL Pvt. Ltd., India. Fluorescent cellular probes, lysotracker green DND-26, and Rhodamine B (RhoB) were procured from life technologies and were used as per manufacture's instruction. 3-(4,5-Dimethylthiazol-2-yl)-2,5-diphenyltetrazolium bromide (MTT) was bought from Amresco life science, USA. PCR primers used in this work were ordered from Imperial Life Science, India. Other chemicals used in this work were analytical grade and were used as received without further modification. A549 (Non-Small Cell Lung Cancer) cells were received from National Centre for Cell Science, Pune, India. They were maintained in Dulbecco's modified Eagle's medium (DMEM) with 10% fetal bovine serum (FBS) and 1% penicillin-streptomycin in 37 °C incubator with 5% CO₂ and 95% air.

Synthesis of bPEI-RhoB Conjugates. The fluorescent RhoB was conjugated to bPEI by EDC and NHS coupling reaction. The free -COOH groups of RhoB were covalently linked to primary amine (-NH₂) groups at the terminal of bPEI by amide bonds. As an initial activation step, free amine groups of bPEI (0.1 g) were deprotonated in the presence of sodium carbonate buffer (brought to pH 6 after gradual addition of 1 mM HCl). Equimolar amounts of EDC and NHS (4 mmol) were added to 20 mL of phosphate-buffered saline (PBS) and were stirred for 20 min at room temperature and then were preincubated at 0 °C for 10 min. To this homogeneous solution, around 80 mg of RhoB was added and magnetically stirred for 2 h. After this, the bPEI solution was added dropwise to this reaction mixture. The reaction mixture was stirred at room temperature for 48 h to allow completion of reaction. The final reaction mixture obtained was then dialyzed (MWCO, 12 kDa) against deionized water for 3 days until a constant fluorescence was observed in dialyzing medium. The resultant RhoB-bPEI conjugate retained within the dialysis tube was then freeze-dried and then was diluted to working concentrations in deionized water.

Synthesis of RBP Polyplexes. RhoB-bPEI-pDNA (plasmid DNA) (RBP) complexes with different N/P ratios were synthesized by adding appropriate volumes of RhoB tagged bPEI to an equivalent amount of pDNA in deionized water. The pDNA and RhoB tagged bPEI mixture was gently mixed and then was incubated at room temperature for 20–30 min to facilitate complete interaction.

DNA Binding Assay. The encapsulation efficiency and stability of polyplexes formed between RhoB modified bPEI and pVITRO2-GFP/CD::UPRT plasmid was evaluated by gel retardation assay at different weight ratios. Different volumes of pDNA (0.4 mg/mL) were added to RhoB modified bPEI (1 mg/mL) in PBS. The mixture was then vortexed for 5 s and then was allowed to stand for 10 min at room temperature in order to facilitate efficient encapsulation. The total amount of DNA was kept constant with varying bPEI concentration in each reaction mixture so as to attain different N/P ratios. Thus, formed DNA-bPEI polyplexes were then loaded in 0.8% (w/v) agarose gel and were run at 65 mV for 45 min. The DNA bands were then monitored under UV illumination by BioRad gel documentation system at appropriate exposure time.

DNase I Protection Assay. The RhoB tagged bPEI ability to circumvent predisposal of encapsulated pDNA to cellular nuclease was assayed by DNase I protection assay. RBP complexes with the same N/P ratios as adapted during encapsulation studies (each with 500 μ g of pDNA) were treated with 0.6 U DNase I for 15 min at 37 °C. After the incubation period, the reaction was terminated by addition of 1.5 mL of ethylenediaminetetraacetic acid (EDTA) (50 mM) followed by inactivation of DNase I enzyme at 65 °C for 15 min. To confirm the intactness of pDNA within the complexes, the encapsulated pDNA was released from the RhoB-bPEI complexes by addition of 3 mL of 4 mg/mL heparin which competitively binds with pDNA. The reaction mixture was allowed to stand at 37 °C for 3 h to ensure complete dissociation of complexes. The pDNA thus released was then assessed by gel electrophoresis (0.8% agarose) at 65 V for 1 h. Bare pDNA processed through identical steps was adapted as experimental control.

Size, Zeta Potential, and Morphology of RBP Complexes. The hydrodynamic radius and surface charge of RBP complexes at optimum N/P ratio was estimated by Malvern Zetasizer Nano ZS90 (Malvern, U.K.) at 25 °C. All data were acquired in monomodal acquisition mode as per Smoluchowski theory. The morphology of RBP complexes was examined by atomic force microscope (AFM-NTEGRA PNL) with Si cantilever (spring constant, 21 N/m) probes operating in semicontact mode at a resonance frequency of 160 kHz. The images were acquired with scan field of 5 μ m \times 5 μ m and then were processed further using NOVA software for size and roughness analysis.

Fabrication of RBP/5-FC Loaded Core-Shell Nanofibers. Standard core-shell electrospinning apparatus procured from ESPIN Nano (Physics Equipment and Company, India) was used for fabrication of core-shell nanofibers. The presynthesized RBP polyplexes (10 mL of RBP at N/P ratio of 3) were concentrated initially by dialysis and then were dissolved in 3.5 wt % PEO and 0.8 wt % bPEI solution in distilled water. After curing the solution for 3–4 h, the polymer blend was fed as shell solution in the electrospinning apparatus. The prodrug 5-FC (0.25 wt %) was added to 3.5 wt % PEO and 1% bPEI in distilled water and was fed as core solution in the electrospinning setup. The coaxial spinneret of electrospinning unit comprised of a 10 gauge inner needle was concentrically positioned within an outer needle of 20 gauge diameter. The solutions were fed into vertical coaxial electrospinning apparatus with two independent programmable peristaltic microsyringe pumps. The spinneret tip was connected to a variable high voltage power supply to dissipate charge into the polymer solution. The instrument was operated at 14 kV. The

flow rate for core and shell drug-polymer blend was maintained at 0.15 mL/h and 0.2 mL/h, respectively. The nanofiber produced in the process was collected over grounded stationary metal collector positioned at a distance of 20 cm from the spinneret. The nanofiber deposition was carried out for a stipulated time under a controlled cabinet temperature of 32 °C and a constant relative humidity of 55%.

Cross-Linking of Core-Shell Nanofibers. The RBP complex and 5-FC loaded core-shell nanofibers were pre-treated with glutaraldehyde (50% v/v) vapor for 10 s in a closed chamber at 40 °C. After glutaraldehyde vapor treatment, the fibers were transferred to a hot air oven at 45 °C for 3 h to remove the remnant unreacted glutaraldehyde from the scaffold. The cross-linked core-shell nanofiber was then UV sterilized for 20 min before being carried over for cell culture studies.

Characterization of Core-Shell Nanofiber. The morphology of 5-FC and RBP complex loaded core-shell nanofiber was observed by Ultra plus-Carl Zeiss field emission-scanning electron microscope (FE-SEM) operating at 5 kV. The fibers were gold coated for 30 s in Denton gold sputter unit before being mounted in FE-SEM. The core-shell nanofiber images were procured and then were further processed by ImageJ software to obtain the mean fiber diameter and fiber diameter distribution. The 5-FC entrapment efficiency was calculated by the following equation:

$$\begin{aligned} \text{entrapment efficiency} \\ = (\text{total mass of drug released from nanofiber} \\ / \text{mass of total drug added}) \times 100 \end{aligned}$$

The total amount of 5-FC loaded in core-shell nanofiber was estimated by disrupting the drug-loaded nanofibers in PBS by probe sonication for 10 min (2 s on and 3 s off). After complete disruption of nanofiber, 5-FC was released into PBS which was later quantified with respect to 5-FC standard plot to arrive at total mass of 5-FC loaded. The degree of swelling and weight loss of core-shell nanofiber when incubated in PBS was estimated by the following equation:

$$\text{degree of swelling}\%(W_s) = (W_1 - W_2)/W_2 \times 100$$

$$\text{weight loss}\%(W_L) = (W_2 - W_3)/W_2 \times 100$$

where W_1 is the weight of the swollen nanofiber, W_2 is the initial weight of the sample before incubation, and W_3 is the weight of the PBS incubated sample after drying at 40 °C.

RBP polyplexes and 5-FC loaded core-shell nanofibers were cross-linked in the presence of glutaraldehyde vapor and were then soaked in PBS (pH 7.2) at 37 °C for 48 h. After the stipulated incubation period, the wet and dry masses of nanofibers were estimated in order to determine the degree of swelling and weight loss.

Drop Shape Analysis System-DSA30 (Kruss, Hamburg, Germany) was used to measure static contact angles sessile drop method. In brief, around 30 μ L of ultrapure water was dropped onto 5-FC and RBP polyplexes loaded core-shell PEO-bPEI nanofiber surface, and the contact angle was calculated after 60 s time span.

The Fourier transform infrared (FTIR) spectra of core-shell nanofibers with different compositions were acquired by Thermo Nicolet spectrometer using KBr pellets in the range 4000–400 cm^{-1} . FTIR spectra of control samples were also

acquired for foolproof interpretation of peaks. TG-DTA analysis of core-shell nanofibers was carried out to assess its composition and stability. About 10 mg of sample was heated from 32 to 550 °C at a constant rate of 10 °C/min in nitrogen atmosphere by EXSTAR TG/DTA 6300.

Release Study of RBP Complex and 5-FC from Core-Shell Nanofibers. RBP and 5-FC loaded core-shell nanofibers (15 mg) were immersed in 5 mL PBS (pH 7.0) for 96 h under static conditions. At each time point, around 100 μ L of release medium was transferred to fresh wells for UV-vis absorbance spectroscopic and fluorescence spectroscopic analysis. The release medium withdrawn at each time point was then replenished with an equivalent amount of fresh medium. Time-dependent release of RhoB tagged bPEI-pDNA complexes was monitored by a corresponding increase in fluorescence (associated with RhoB) in the release medium. An excitation wavelength of 510 nm was used, and emission spectra were acquired from 540 to 700 nm with an interval of 5 nm by Cytation3 multimode reader (Biotek Instruments, Inc.). The obtained fluorescence maximum value at 565 nm was normalized with respect to fluorescence values obtained for un-cross-linked RBP and 5-FC loaded core-shell nanofiber to arrive at percentage release of complex. Corresponding 5-FC release with respect to time was quantified by acquiring absorbance at 276 nm by UV-vis spectrophotometer and by correlating it to standard plot. All samples in the experiment were in triplicates. The results were represented in terms of cumulative percentage drug release.

$$\text{cumulative percentage of 5-FC released} = M_t/M_{\infty} \times 100$$

where M_t is mass of 5-FC released at time t and M_{∞} is total mass of 5-FC loaded in the nanofiber.

pH Dependent Fluorescence Stability of RBP Complexes. The pH dependent fluorescence stability of RhoB tagged to bPEI in pDNA polyplexes was quantified at different pHs (pH 1–11) by Cytation3 multimode reader (Biotek Instruments, Inc.). The polyplexes were excited with 510 nm laser, and subsequent emission spectra were acquired starting from 540 to 700 nm with intervals of 5 nm.

RBP Uptake Studies. Owing to fluorescence properties of RhoB tagged to bPEI-pDNA polyplexes, its cellular uptake was monitored in real-time basis by fluorescence microscopy (EVOS FL Color, AMEFC 4300). Around 1×10^5 A549 cells were seeded over RBP and 5-FC loaded core-shell PEO nanofibers in three separate wells. Each well was terminated at different time points (i.e., 4, 12, and 16 h) and then was monitored under a fluorescence microscope in order to observe time-dependent cellular uptake and localization of RBP polyplexes. After the destined time span of incubation, the spent media was aspirated from the wells and was replaced with 2 mL PBS containing 2 μ L of Hoechst 33342 (stock, 10 mg/mL) and 5 μ L LysoTracker green (stock, 50 mM). The cells were incubated at 37 °C for 30 min for proper uptake of dyes and then were fixed by 2% glutaraldehyde solution for 5 min. After glutaraldehyde, fixation cells were monitored under fluorescence microscope using DAPI filter (Hoechst 33342 stained nucleus), green filter (LysoTracker green stained lysosomes), and red filter (RhoB labeled bPEI-pDNA polyplexes).

Time-Dependent Transfection of Suicide Gene (GFP/CD::UPRT). The fraction of A549 cells transfected with GFP/CD::UPRT suicide gene at different time points were initially observed under fluorescence microscope (EVOS FL Color,

AMEFC 4300) and were further quantified by flow cytometry (Amnis FlowSight). Around 1×10^5 A549 cells were seeded over RBP loaded core-shell nanofibers in a six-well plate. At 20, 28, 34, and 48 h, the media in the respective wells was removed and replaced with 2 mL PBS containing 1 μ L of Hoechst 33342 (10 mg/mL) and was incubated for 5 min. After incubation time, the excess stain was washed with fresh PBS and then was visualized under a fluorescence microscope. Images were acquired under DAPI filter (Hoechst 33342 stained nucleus) and green filter (autofluorescent core-shell nanofibers) and were processed further to generate overlay of two images. After microscopic observation, the same batch of cells was trypsinized and resuspended in PBS for quantification of transfected cells by flow cytometry. The GFP/CD::UPRT expressing green fluorescent transfected cells were distinguished from untransfected cells by exciting green fluorescent protein by 488 nm laser. A plot of normalized frequency % with green fluorescence intensity in channel 2 (Intensity_MC_Ch02) was generated after acquiring 10 000 events for each sample.

Suicide Gene Bystander Effects. To assess the bystander effects of CD::UPRT suicide gene therapy, a combination of propidium iodide and Hoechst 33342 stain was adapted. A549 cells pretreated with RBP and 5-FC loaded core-shell nanofibers were withdrawn from culture condition at 48, 72, and 96 h and were stained with Hoechst 33342 (1 μ L from 10 mg/mL stock) and PI (10 μ L from 1 mg/mL stock) in PBS. The cells were incubated at 37 °C for 30 min after which the excess stain was gently washed away with PBS. Images were acquired under DAPI filter, green filter, and red filter and then were overlaid to identify dead, live, transfected, and non-transfected cells.

Cell Viability Assay. Cell lines A549 and L-132 were obtained from the cell repository of National Centre for Cell Science, India. Cells were maintained in DMEM (high glucose) medium supplemented with 10% FBS, 50 U/mL penicillin, and 50 mg/mL streptomycin in a humidified atmosphere in 5% CO₂ at 37 °C. The core-shell nanofibers' ability to deliver suicide gene to cancer cells and subsequently to mediate catabolic conversion of prodrug 5-FC into toxic byproducts was assessed initially by cell viability (MTT) assay as mentioned elsewhere.¹⁰

Two different concentrations of 5-FC (0.25 and 0.5 wt %) and RBP were loaded in core-shell nanofibers in order to generate four different versions of core-shell nanofibers. Core-shell NF1 and core-shell NF2 were loaded with the same extent of RBP polyplexes in the shell but with 0.25 and 0.5 wt % of 5-FC in the respective nanofiber core. Similarly, core-shell NF3 and core-shell NF4 were loaded with different amounts of RBP polyplexes in the shell but with the same amount of 5-FC (i.e., 0.25 wt %).

Semi-Quantitative Reverse Transcription Polymerase Chain Reaction (RT-PCR). Suicide gene transfection and its subsequent expression by A549 cells were estimated by semiquantitative RT-PCR. Furthermore, the differential expression of apoptotic genes that arises in later stages of suicide gene therapy was also monitored by RT-PCR. The total RNA was extracted from A549 cells subjected to suicide gene therapy at predestined treatment duration by Tri reagent (Sigma-Aldrich, USA). The cDNA was generated by reverse transcription of 3 μ g of total denatured RNA using M-MLV reverse transcriptase (Sigma, USA). The cDNA product was used for gene-specific amplification of GFP/CD::UPRT and other

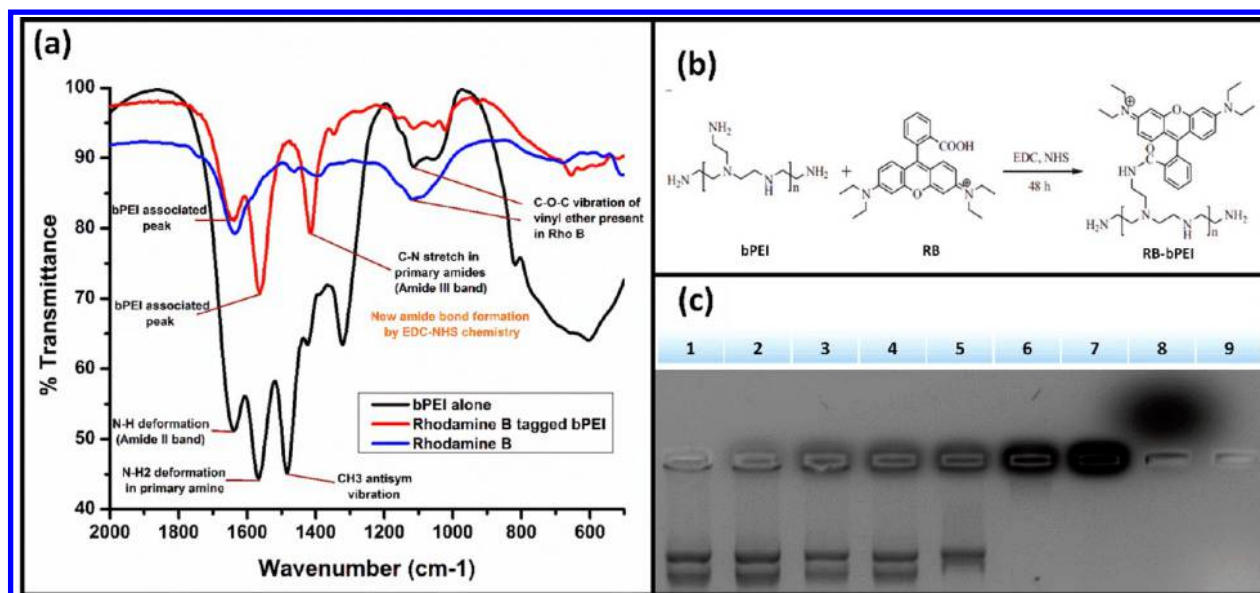


Figure 1. RhoB-bPEI synthesis (a) FTIR spectroscopy and (b) schematic, (c) gel retardation assay of RhoB tagged bPEI-pDNA polyplexes (lane 1, bare pVITRO2-GFP/CD::UPRT plasmid; lane 2, lane 3, lane 4, lane 5, and lane 6 loaded with RBP polyplexes of N/P ratios of 0.5, 1, 1.5, 2, and 3, respectively; lane 7, bare RhoB tagged bPEI; lane 8, RhoB alone; and lane 9, bPEI alone).

apoptotic genes. The forward and reverse primers utilized for PCR amplification are mentioned in Table S1. Beta-actin (housekeeping gene) was adapted as an internal control. The PCR products were finally resolved in 1% agarose gel and were visualized by ethidium bromide staining under UV light. The difference in gene expression was computed from the gene-specific bands obtained by Image lab 4.0 software. The apoptotic genes considered for gene expression studies include *bad*, *bak*, *bax*, *p53*, *caspase-3*, and *C-myc*; apart from these, antiapoptotic genes *bcl-2* and *bcl-XL* were also included in the study.

Flow Cytometry Analysis of Suicide Gene Therapy.

The cascade of events that fosters GDEPT was assessed by flow cytometry at different time points. A549 (1×10^5 cells) cells were seeded over RBP and 5-FC loaded core-shell nanofibers and were analyzed at 24, 36, and 72 h. After the respective incubation period, cells were trypsinized and resuspended in PBS (200 μ L); to each of the samples, 10 μ L of PI was added, and then the cells were incubated at 37 $^{\circ}$ C for 20 min. The samples were loaded in flow cytometry (Amnis Flowsight), and upon excitation by 488 nm laser, green fluorescence of transfected cells and red fluorescence of PI stained dead cells could be observed in different channels. Around 10 000 events were acquired for each sample and then were analyzed by Amnis Ideas software to arrive at percentage transfected cells and dead cells at different time points.

FE-SEM Analysis of Cellular Morphology. The release of RBP polyplexes from nanofibers and its attachment over cell surface was observed by FE-SEM during the initial period of incubation. Apart from this, subsequent morphological changes manifested by A549 cells seeded over RBP and 5-FC loaded core-shell PEO nanofibers were also clearly discerned under FE-SEM. Treated A549 cells over nanofibrous scaffold were given mild PBS wash and then were fixed with 2% glutaraldehyde solution for 5 min. The remnant glutaraldehyde was washed away by ethanol/water gradient and then was air-dried for 5 min before being observed under FE-SEM.

3. RESULTS AND DISCUSSION

3.1. Synthesis of RhoB Tagged bPEI-pDNA Polyplexes. The efficient conjugation of RhoB to bPEI by EDC/NHS chemistry was confirmed by FTIR and gel retardation assay. During the course of reaction, $-\text{COOH}$ groups of the RhoB were covalently bonded to $-\text{NH}_2$ (primary amine) groups of bPEI by amide bonds. A reaction scheme for this process is depicted in Figure 1b. The FTIR spectra of bPEI had peaks at 1481 cm^{-1} (corresponding to antisymmetric stretch of CH_2 in aliphatic compounds) and sharp peaks at 1567 and 1637 cm^{-1} ascribed to N-H deformation in primary amines and amide II band, respectively (Figure 1a). IR spectra of RhoB possessed a characteristic absorption peak at 1630 cm^{-1} corresponding to $\text{C}=\text{N}$ stretch vibration and another peak at 1467 cm^{-1} corresponding to the presence of benzene rings (ring stretch vibration).¹¹ FTIR spectra of RhoB tagged bPEI possessed characteristic peaks of bPEI (1567 and 1637 cm^{-1}) and RhoB (1114 and 1087 cm^{-1}). Apart from these, an additional strong peak at 1413 cm^{-1} was observed in RhoB tagged bPEI, which arises because of C-N stretch of primary amides (amide III band) that was formed by EDC-NHS coupled reaction between COOH group of RhoB and terminal NH_2 group of bPEI.

Apart from FTIR analysis, RhoB conjugated bPEI synthesis was confirmed further by gel retardation assay, as RhoB presence could also be monitored under UV. During agarose gel electrophoresis, free RhoB migrates toward the anode (lane 8) under the influence of external field whereas RhoB conjugated to bPEI was retained in the loading well itself (lane 7) (Figure 1c). The higher molecular weight and hyperbranched structure of bPEI limit its mobility during electrophoresis, and as a consequence, RhoB conjugated to bPEI was also retained in the well. A concentration-dependent increase in RhoB-bPEI intensity was also observed in subsequent wells with increasing N/P ratio (lanes 1–6) (Figure 1c). At N/P ratio of 7, pDNA was completely condensed to form stable polyplexes wherein DNA's negative charge was completely masked by amine groups of bPEI

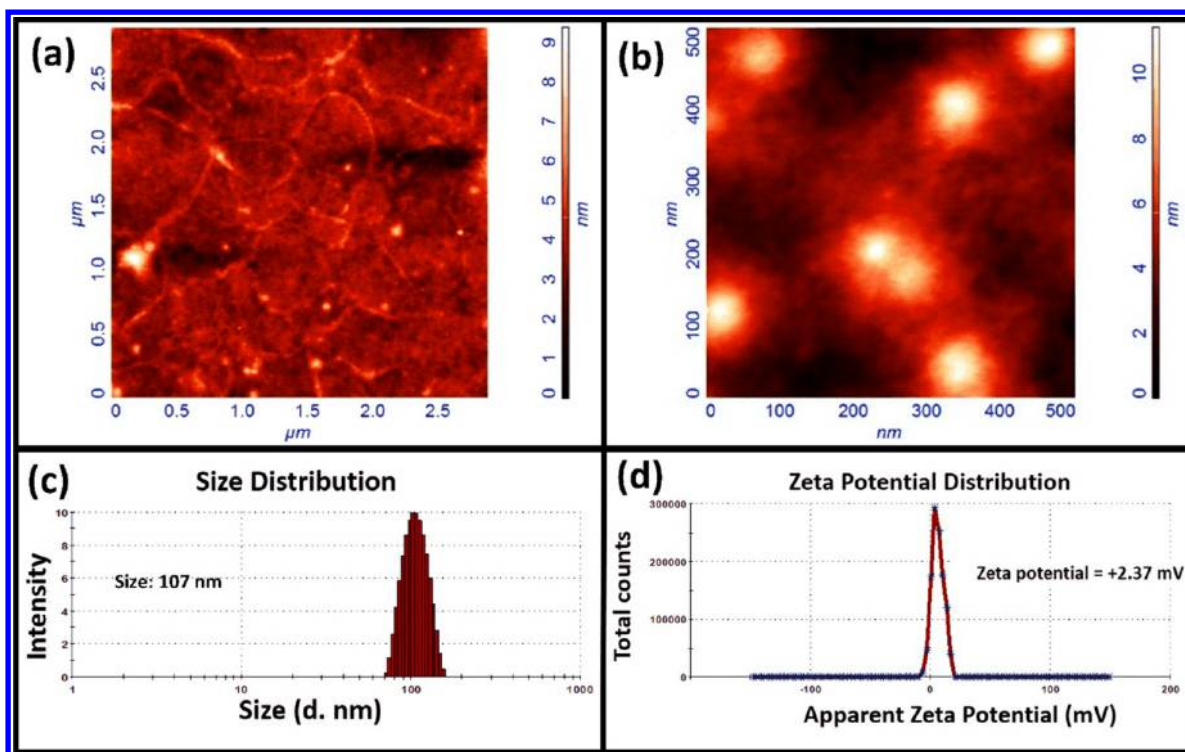


Figure 2. AFM image of (a) pVITRO2-GFP/CD::UPRT plasmid and (b) RBP polyplexes. (c) Size distribution and (d) zeta potential of RBP polyplexes.

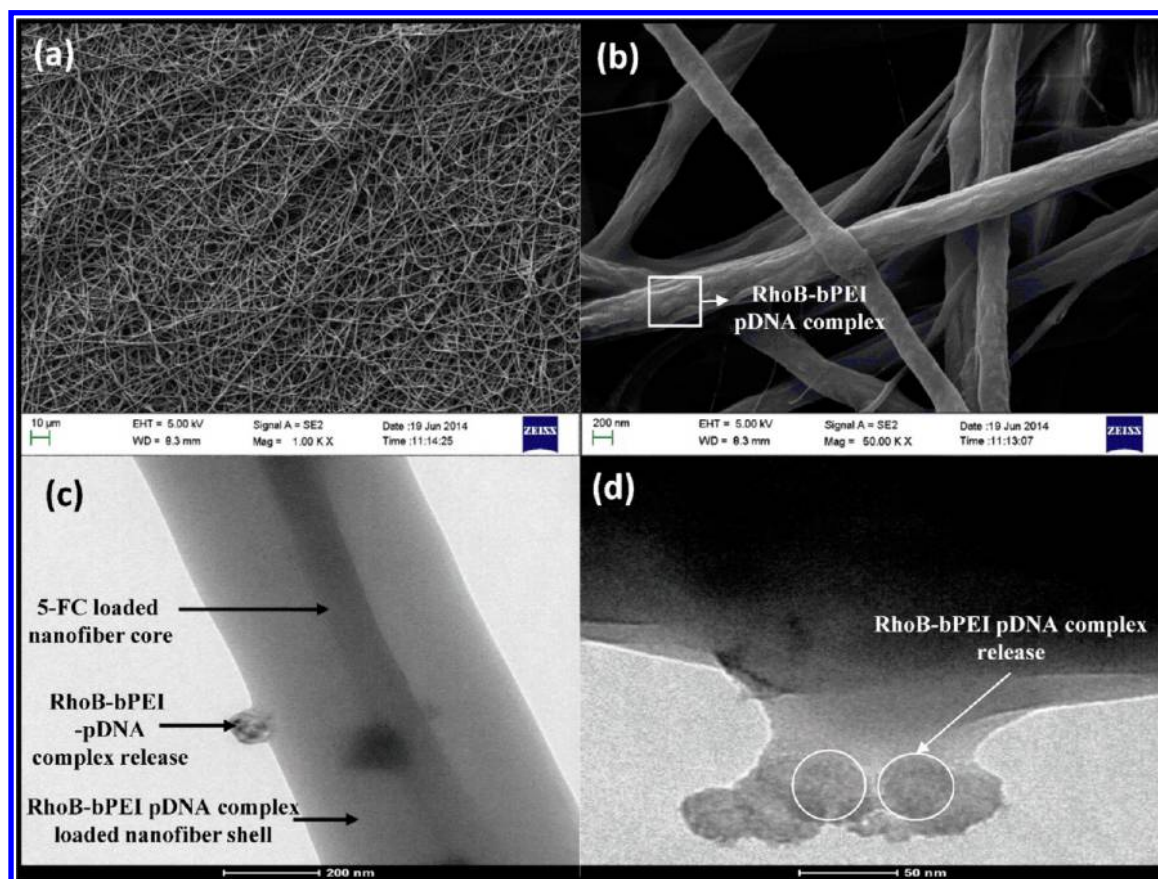


Figure 3. FE-SEM image of RBP and 5-FC loaded core-shell nanofibers (a) at lower magnification to depict uniform fiber distribution, (b) at higher magnification in order to visualize partial demarcation of RBP polyplexes on the surface; (c) TEM images of core-shell nanofibers showing intact core-shell morphology and (d) gradual release of RBP polyplexes from nanofibers.

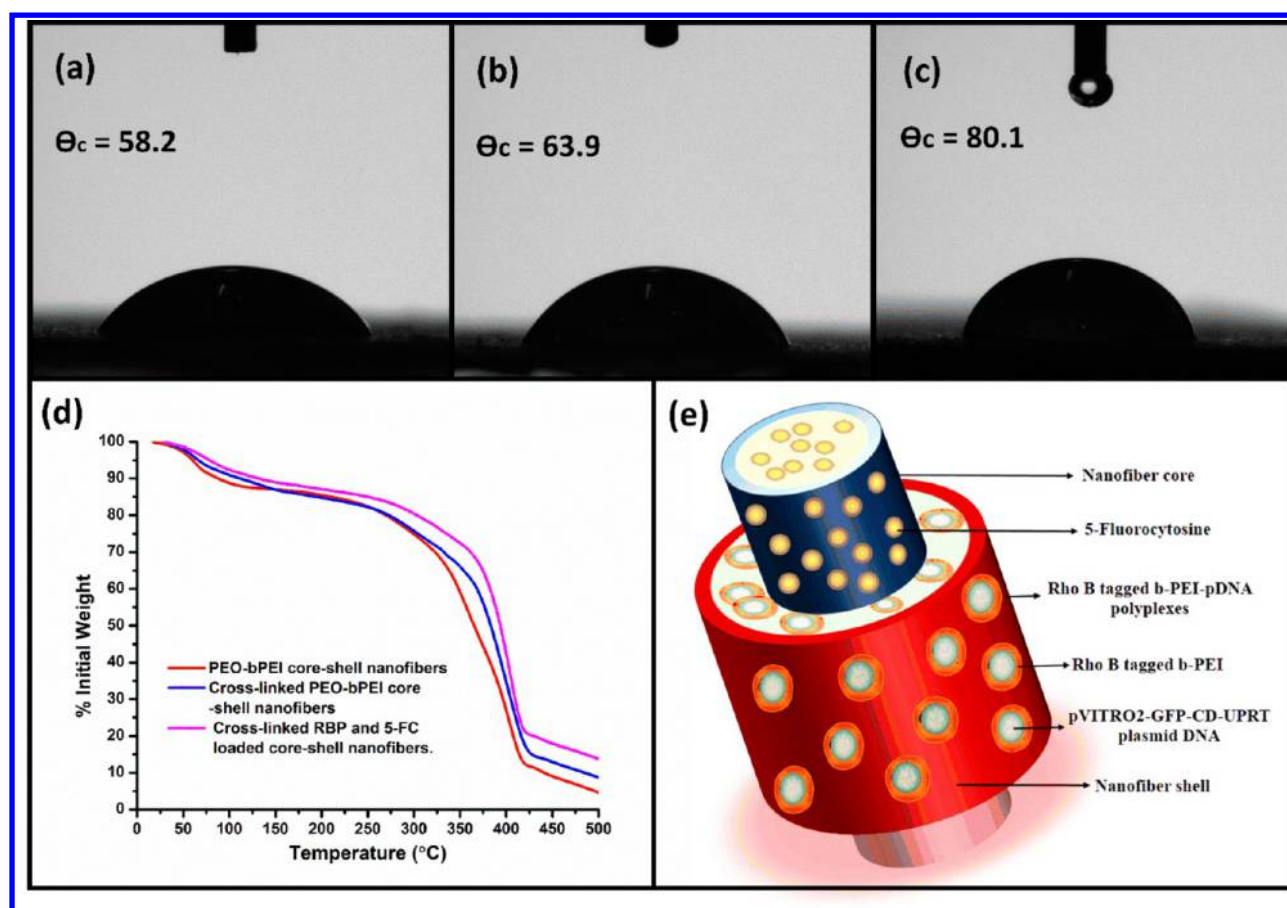


Figure 4. Water contact angle measurement for (a) bare PEO-bPEI core-shell nanofibers, (b) RBP polyplexes and 5-FC loaded core-shell nanofibers, and (c) glutaraldehyde cross-linked core-shell nanofibers loaded with RBP polyplexes and 5-FC; (d) TGA of different versions of core-shell nanofibers; (e) illustration of core-shell nanofibers loaded with RBP polyplexes and 5-FC.

because these polyplexes were retained in loading wells even under applied external field. The atomic force microscopy (AFM) of RBP polyplexes (N/P ratio 7) indicated condensed complexes of uniform size distribution in the range of 78–90 nm (Figure 2b). Furthermore, the integrity of plasmid DNA released from RBP polyplexes was also established by AFM (Figure 2a). Thus, formed RBP complexes were distinct with minimal intercomplex interaction which suggests better stability and intactness of polyplexes. The hydrodynamic size distribution of RBP polyplexes was estimated to be ~ 107 nm (mean diameter) by dynamic light scattering (DLS) measurement which was in coherence with AFM images (Figure 2c). The polyplexes' zeta potential in aqueous solution was estimated to be $+2.37$ mV owing to excessive free amine groups of bPEI present on its surface. RhoB tagged to bPEI moieties is also positively charged, and thus, it contributes partially to positive zeta potential of the polyplexes (Figure 2d). Bare bPEI polyplexes with pDNA at the same N/P ratio (i.e., 7) were observed to have marginally higher zeta potential of 3.15 mV as few amine groups of bPEI were consumed in amide bond formation during RhoB conjugation. The integrity of pDNA in the RBP polyplexes on predisposal to intracellular DNase enzymes was confirmed by DNase I protection assay (Figure S1). The lane 1 indicates control plasmid at the same concentration as used for encapsulation followed by negative control where free DNA is completely degraded by DNase I. In subsequent lanes, that is, lanes 3–5, bands corresponding to intact plasmid present within RBP polyplexes were observed.

The increasing plasmid intensity with higher fraction of bPEI in RBP polyplexes clearly indicates that a higher proportion of bPEI could effectively mask a greater fraction of pDNA from DNase I mediated degradation.

3.2. Characterization of Core-Shell Nanofibers Loaded with RBP Polyplexes and 5-FC.

The FE-SEM observation of electrospun core-shell PEO nanofibers loaded with RBP and 5-FC indicated uniform fiber diameter distribution of 350 ± 58 nm (Figure 3a). Core-shell nanofiber images at higher magnification under FE-SEM revealed partial demarcation of spherical RBP polyplexes present in the nanofiber shell layer (Figure 3b). As distinctly visible under FE-SEM, these polyplexes were incorporated uniformly within nanofibers and remained intact in shape and morphology even after electrospinning. The core-shell morphology of nanofibers could be discerned clearly under TEM wherein the nanofiber core loaded with 5-FC generated a clear contrast with the shell layer loaded with RBP polyplexes (Figure 3c). The TEM image of RBP and 5-FC loaded core-shell nanofiber in Figure 3c, d indicates the event of polymer dissolution from the nanofiber shell layer and gradual elution of RBP polyplexes from the nanofibers during the initial phase of PBS incubation. Prodrug 5-FC loaded within the nanofiber core remains intact with minimal diffusion during the initial phase. This time lag attained between release of two components (i.e., RBP and 5-FC) is considered favorable for fostering efficient suicide gene therapy.¹³ Postfabrication cross-linking of core-shell nanofibers with glutaraldehyde limits dissolution of RBP to a great extent.

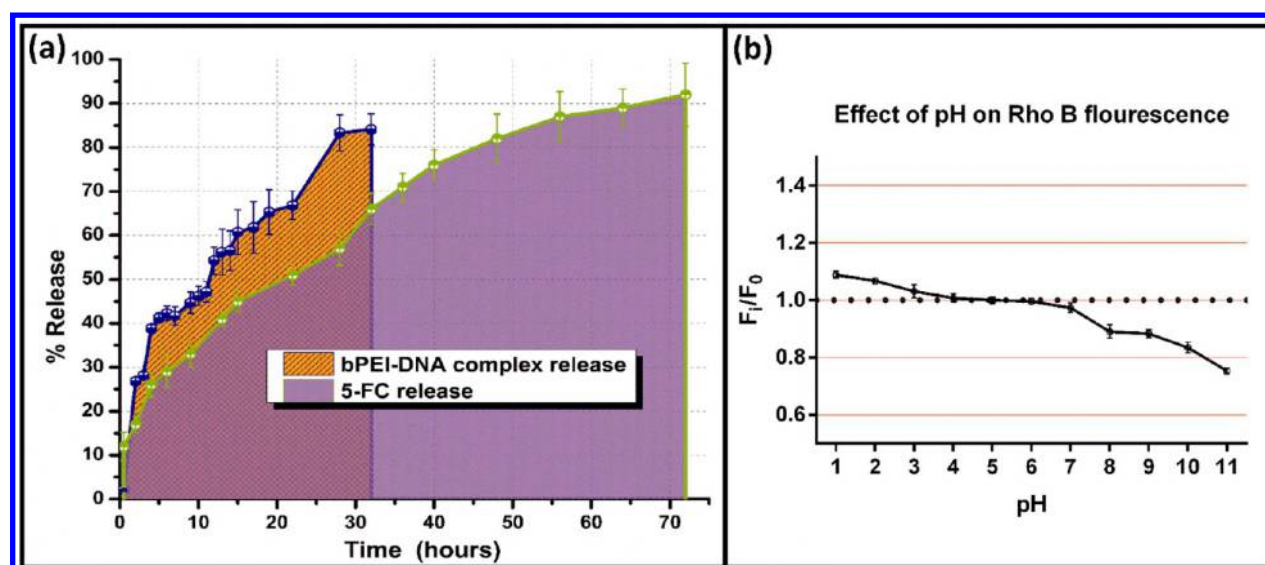


Figure 5. (a) Release profile of RBP polyplexes and 5-FC from core-shell nanofibers; (b) effect of pH on RhoB fluorescence.

The presence of a small fraction of primary amines on the surface of RBP extends a possibility of generating cross-links with free bPEI present in the matrix of the nanofiber.¹⁴ The presence of such cross-links may at times strip off a small fraction of bPEI during the course of RBP dissolution and thereby reduce the polyplex diameter to a certain extent as observed in Figure 3d. The presence of such cross-links also leads to extrusion of the polymer matrix along with dissolving RBP into the release medium (Figure 3d).

Core-shell nanofibers being hydrophilic in nature tend to exhibit polymer swelling and dissolution with respect to time of incubation in hydrophilic environment. The degree of cross-linking determines polymer swelling and dissolution. This hypothesis was confirmed when core-shell nanofibers with higher bPEI content (i.e., 1.2 wt %) were observed to undergo lower weight loss (i.e., 26.1%) and polymer swelling (i.e., 31.7%) as compared to core-shell nanofibers with lower bPEI content (i.e., 0.8 wt %) for which weight loss and polymer swelling was estimated to be 33.4% and 37.3%, respectively.

Contact angle analysis of core-shell nanofibers clearly depicted their hydrophilic nature (contact angle < 90°) owing to the presence of hydrophilic components PEO and bPEI (Figure 4a–c). The bare core-shell nanofibers possessed a contact angle value of 58.2° which increases slightly to 63.9° upon loading with RBP and 5-FC in core and shell of the nanofibers, respectively. Subsequently, partial glutaraldehyde mediated cross-linking of nanofibers imparts it better stability in a hydrophilic environment which led to a corresponding increase in the contact angle value to 80.1°. The cross-linked nanofibers being stable in hydrophilic environment could retain water which also contributes to an increase in the contact angle values.

The effect of cross-linking and drug loading on thermal stability of core-shell nanofibers was assessed by thermal gravimetric analysis (Figure 4d). The % weight loss of nanofibers with respect to temperature was plotted to distinguish different regimes of polymer and drug degradation. Three different versions of core-shell nanofibers were adapted for this study, that is, un-cross-linked bare PEO-bPEI core-shell nanofibers, cross-linked bare PEO-bPEI core-shell nanofibers, and cross-linked RBP and 5-FC loaded core-shell

nanofibers. A common phase of initial mass loss was observed (up to 65 °C) in all three cases which is ascribed to loss of adsorbed moisture content. At higher temperature regimes, cross-linked nanofibers exhibited better thermal stability as compared to its un-cross-linked counterpart. Glutaraldehyde mediated interchain imide cross-links generated between amine groups of bPEI render the core-shell nanofibers thermal stability.¹⁴ A schematic representation of glutaraldehyde mediated bPEI cross-linking is shown in Figure S2. The drastic loss in mass between 255 and 320 °C is said to arise because of thermal decomposition of free amine groups of bPEI moiety. The long hydrocarbon chains of PEO begin to degrade gradually at 350 °C, and subsequent mass loss was observed up to 520 °C in all three cases. The weight loss profile was observed to be uniform throughout without any abrupt fluctuations indicating the uniform distribution of drug and RBP polyplexes in the polymer phase. A schematic representation of RBP polyplex and 5-FC loaded core-shell nanofiber fabricated in this work is provided in Figure 4e.

3.3. Release of RBP Polyplexes and 5-FC from Core-Shell Nanofibers. Simultaneous release of RBP polyplexes and prodrug 5-FC from the nanofibrous scaffold was quantified and represented as percentage release with respect to time (Figure 5a). It was observed that at the end of 32 h, almost 85% of RBP polyplexes loaded in the nanofiber shell was released whereas only 65% of 5-FC loaded in nanofiber core was released in the meantime. The RBP complexes loaded in the nanofiber shell layer were released during the initial phase of incubation followed by controlled and sustained release of 5-FC loaded in the core of the nanofibers. This time lag between release of RBP from the nanofiber shell and 5-FC from the nanofiber core is said to arise because of two different factors, one is their core/shell localization and the other is the extent of cross-linking. The nanofiber core solution was initially supplemented with glutaraldehyde (0.05 vol %) which led to a higher extent of cross-linking in polymer matrix in order to attain a prolonged release of prodrug 5-FC from the nanofibers.¹⁴ Thus, the distinct release profile of RBP polyplexes (i.e., suicide gene) and prodrug is handy in fostering higher therapeutic efficacy of suicide gene therapy. The RBP polyplexes incorporated within the nanofiber shell layer begin

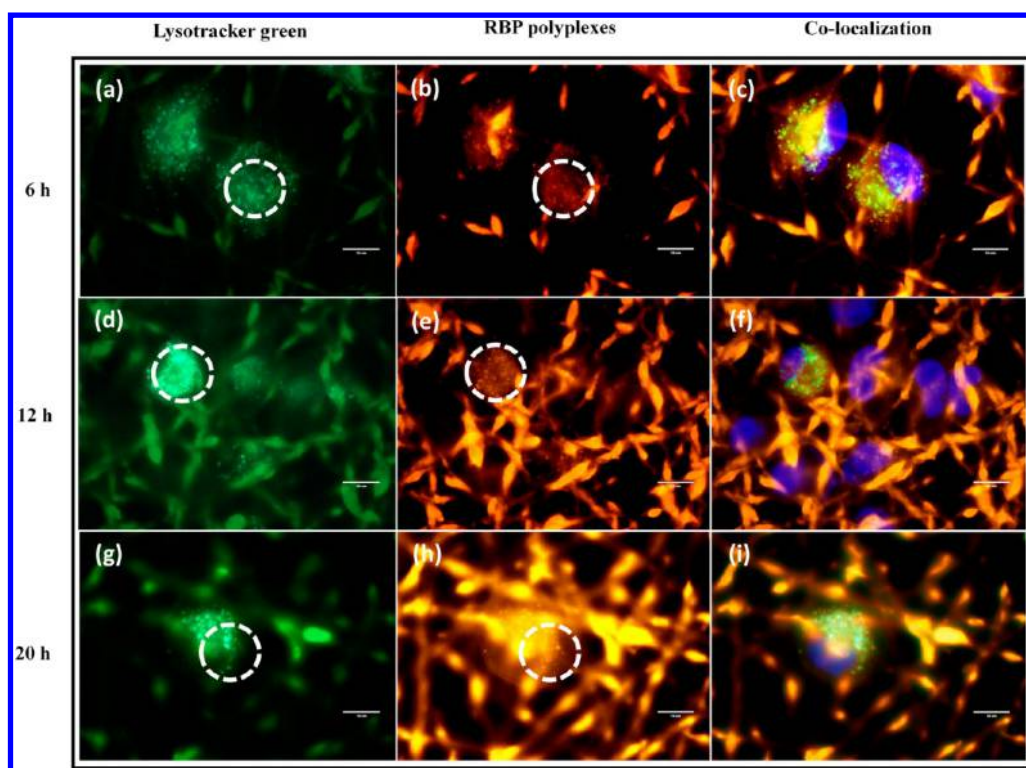


Figure 6. RhoB tagged bPEI-pDNA polyplexes (column 2) colocalization (column 3) within lysotracker green labeled (column 1) lysosomes at 6 h (a–c), 12 h (d–f), and 20 h (g–i).

to surface after gradual dissolution of PEO (Figure 3b). The event of PEO dissolution and subsequent release of RBP in the hydrophilic environment is a dynamic process involving solvent penetration and polymer dissolution at two different fronts. The RBP polyplexes released from the nanofibers were taken up by A549 cells in the vicinity which upon transfection expressed GFP and CD::UPRT genes. These transfected cells expressing the suicide gene were subsequently predisposed to prodrug 5-FC released in the later stages. Almost 91% of 5-FC loaded in the core–shell nanofibers was released by the end of 72 h which was then metabolically converted into toxic byproducts when acted upon by the suicide gene expressed in the transfected cells. At the outset, core–shell nanofiberous scaffold fabricated in the present study could subsequently release RBP polyplexes and 5-FC in a controlled and sustained manner thus extending the scope for eliminating cancer cells by GDEPT.

3.4. pH Dependent Fluorescence Properties of Rho-bPEI Conjugates. RhoB conjugated to bPEI present in the polyplexes serves as a probe to monitor RBP release from the core–shell nanofibers and also aids in tracking its fate following cellular uptake. Previous literature indicates that PEI based carriers end up in highly acidic lysosomes immediately after cellular uptake.⁷ Thus, to monitor the intracellular fate of RhoB tagged bPEI-pDNA polyplexes, its fluorescence stability with respect to pH was evaluated. It was observed that with a fall in pH there was considerable increase in fluorescence emission of RhoB and vice versa (at $\lambda_{\text{max}} = 575 \text{ nm}$, $\lambda_{\text{exc}} = 530 \text{ nm}$). In acidic medium, the amine group of bPEI was completely protonated thereby predisposing tagged RhoB to highly acidic conditions. The dye RhoB was present in a spirocyclic structure which exhibits protonation dependent fluorescence properties.¹² In acidic conditions, the spirocyclic structure of RhoB opened up, which manifests an increase in fluorescence,

whereas in basic conditions, it was deprotonated leading to ring closure leading to a corresponding decline in fluorescence (Figure 5b). Thus, fluorescent RhoB-bPEI conjugate system can effectively track intracellular localization of RBP complexes.

3.5. RBP Polyplex Cellular Uptake Studies. Owing to positively charged amine groups (of bPEI) present on the surface of RBP polyplex, they tend to adhere to the cellular membranes after being released from core–shell nanofibers.¹⁵ It was observed that immediately after adherence of RBP polyplexes over a cellular membrane they were internalized into the cells by endosomes. The event of endosome uptake of RBP polyplexes and its fusion with lysosome was monitored in real time by monitoring fluorescent RhoB tagged to RBP polyplexes under a fluorescent microscope (Figure 6b, e, and h). As observed in the overlay of images, during the initial stages of polyplexes uptake, RBP polyplexes were not localized at the same position as the lysotracker green labeled lysosomes (Figure 6c, f, and i) which depicted the event of endosomal uptake. After 12 h, endosomes carrying RBP polyplex were observed to fuse with lysotracker green labeled lysosomes. The colocalization of red fluorescent RhoB in polyplexes with green fluorescent lysosomes confirmed the event of endolysosome fusion. The presence of protonophoric amine groups of bPEI in RBP polyplexes led to acidification of lysosomes which was followed by their lysis by proton sponge effect.¹⁶

3.6. Transfection of A549 Cells with Suicide Gene in RhoB Labeled bPEI-pDNA Polyplexes. The expression of CD::UPRT suicide gene in transfected A549 cells was monitored by GFP expression under fluorescence microscope in a time-dependent manner. Both nontransfected and transfected cells were stained with Hoechst 33342, whereas only GFP/CD::UPRT transfected cells expressed GFP. The overlay of fluorescent images acquired in DAPI filter and green filter clearly indicated relative fractions of transfected and

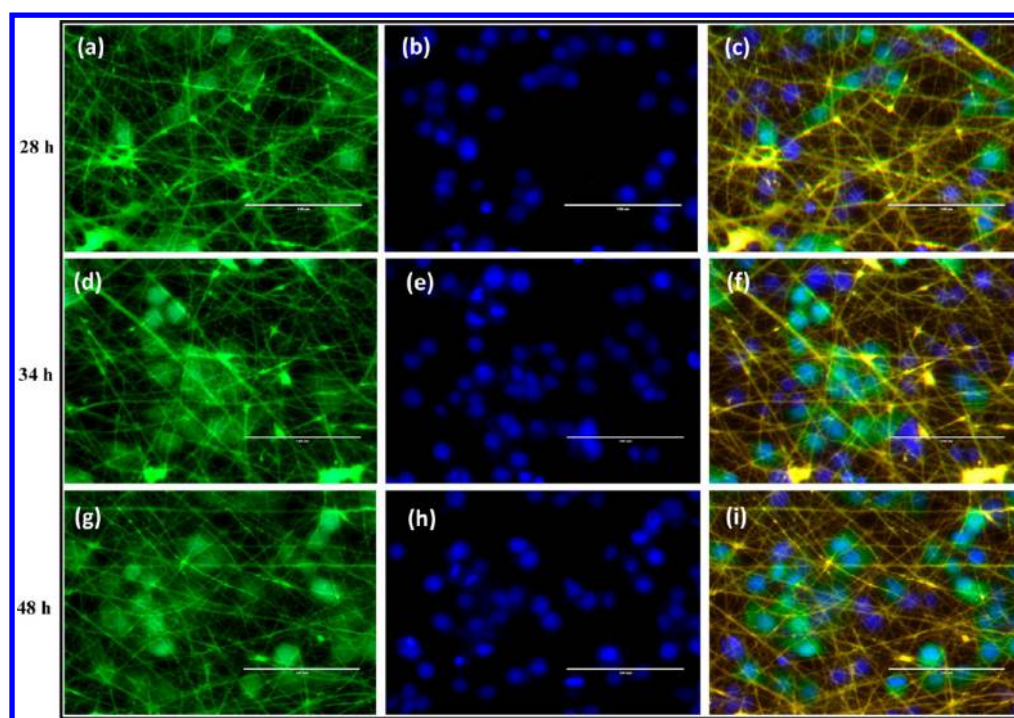


Figure 7. GFP expressing (column 1) suicide gene transfected A549 cells seeded over RBP and 5-FC loaded core–shell nanofibers and Hoechst 33342 labeled live cells (column 2) at (a, b) 28 h; (d, e) 34 h; and (g, h) 48 h. (c, f, i) Overlay of images at respective time points depicts fraction of transfected cells.

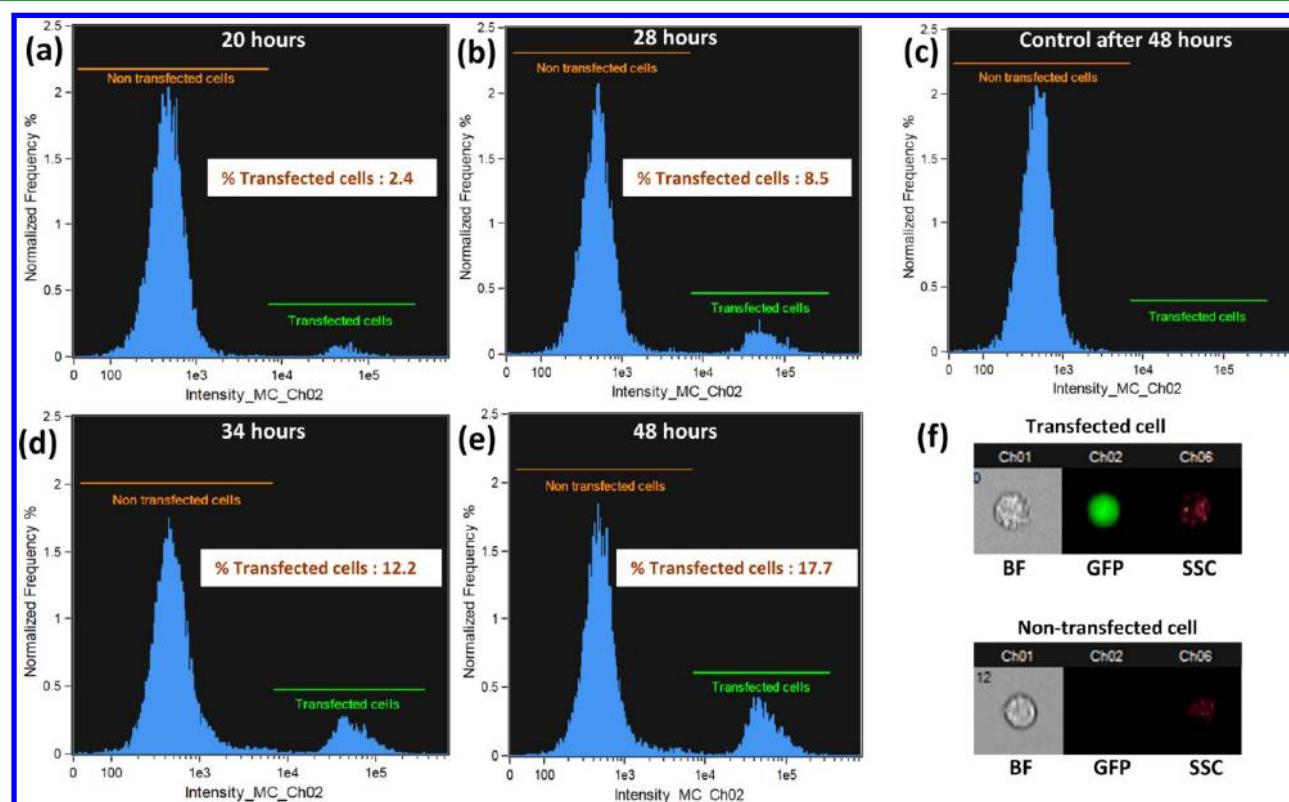


Figure 8. Percentage of A549 cells transfected with GFP/CD::UPRT plasmid after seeding them over RBP and 5-FC loaded core–shell nanofibers at (a) 20 h, (b) 28 h, (d) 34 h, (e) 48 h, and (c) after 48 h seeding over bare core–shell nanofibers; (f) representative images of transfected and nontransfected cells in different channels.

nontransfected cells at different time points. To assess the efficiency of transfection core–shell nanofibers loaded with RBP, polyplexes alone were used in this study. As expected, the

relative fraction of A549 cells expressing suicide gene increased with respect to time (Figure 7). To further complement fluorescent microscopic observation, the treated cells were

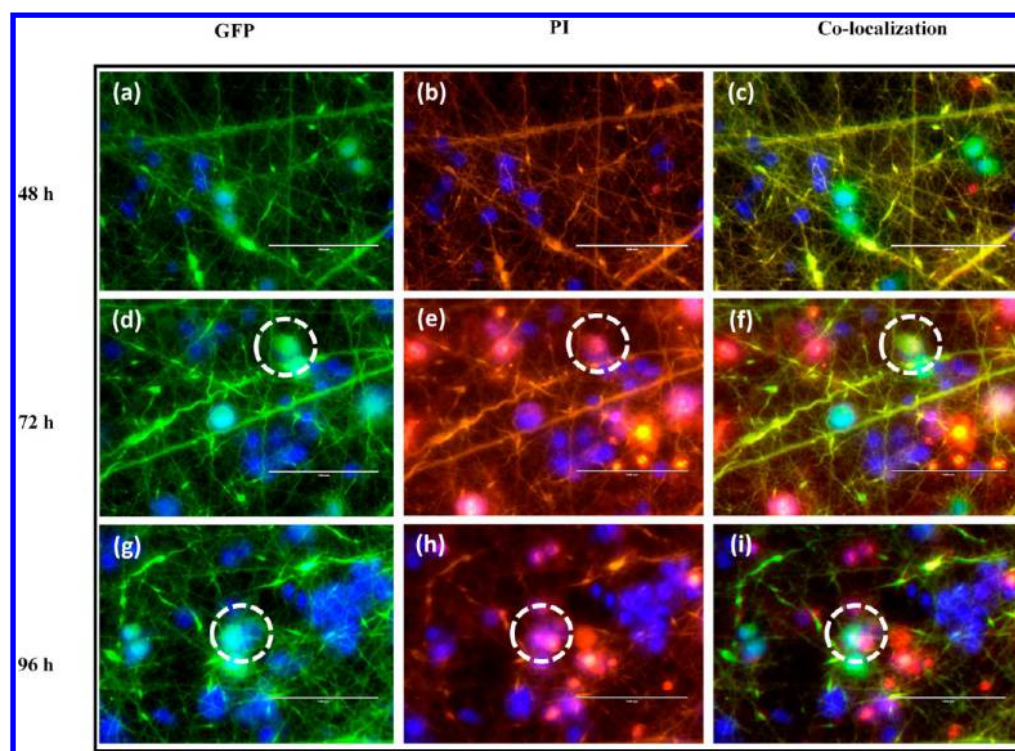


Figure 9. Bystander effects monitored by classifying cell population as (a, d, g) GFP expressing transfected or nontransfected at 48, 72, and 96 h, respectively, and (b, e, h) PI stained dead or live cell. (c, f, i) Overlay of both GFP filter and red filter to identify the dead cells as suicide gene transfected cell or nontransfected.

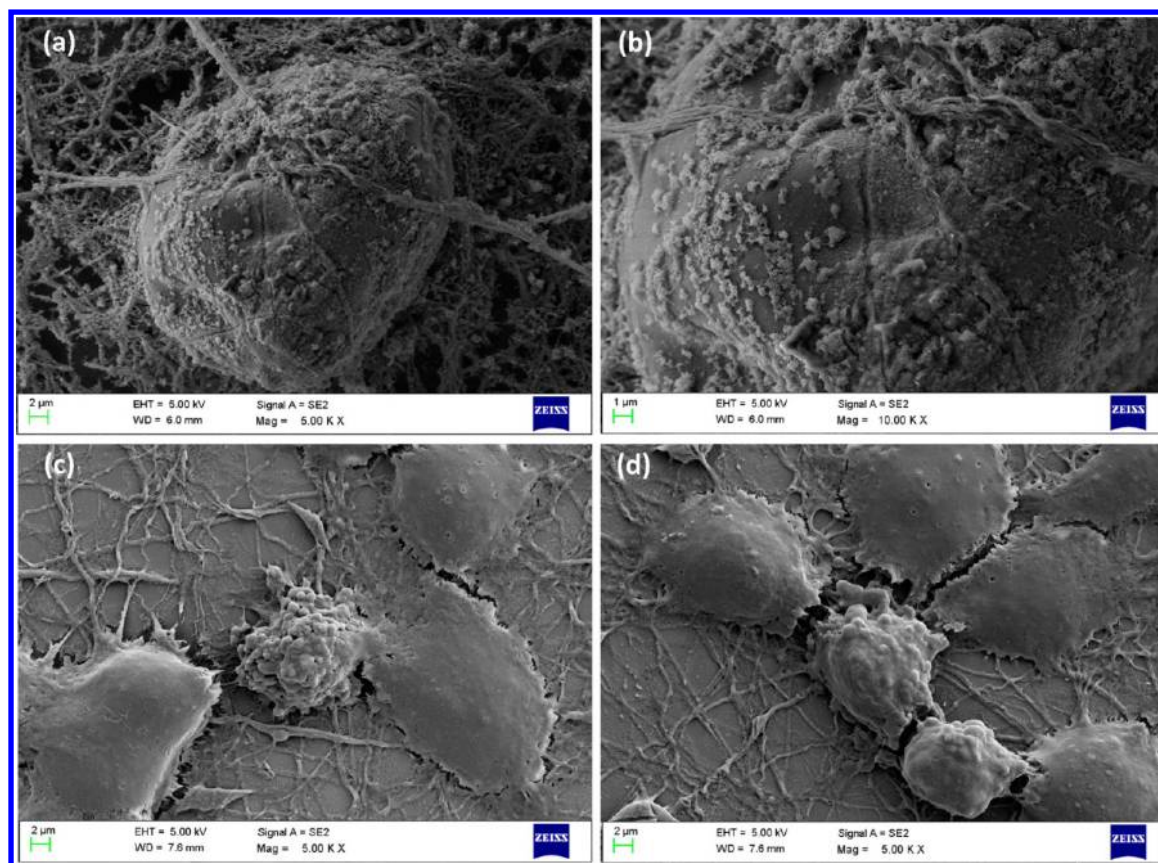


Figure 10. FE-SEM images of A549 cells seeded over core–shell nanofibers indicating events of (a, b) RBP polyplex attachment over A549 cells, (c, d) apoptotic A549 cells at 72 h.

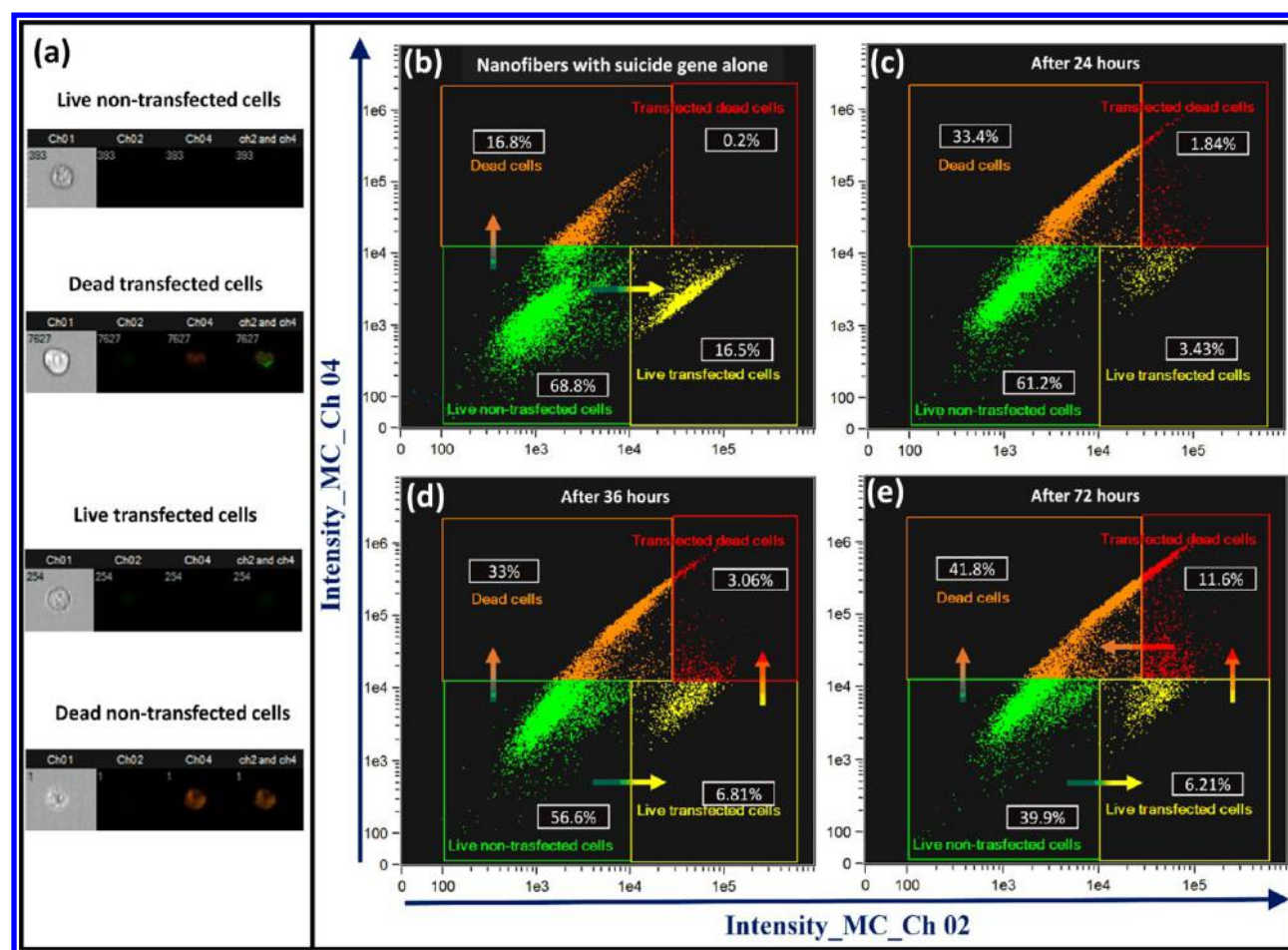


Figure 11. Flow cytometry (a) images of diverse A549 populations as observed in different channels; analysis of A549 cells seeded over (b) control nanofibers with RBP alone at 72 h and (c) core-shell nanofibers loaded with RBP and 5-FC at 24 h, (d) 36 h, (e) 72 h.

analyzed by flow cytometer for GFP expression (% transfected cells) after respective time points (Figure 8). The representative images of A549 cells in each channel for both transfected and nontransfected cells were acquired with appropriate gating of cell population. The transfected cells were monitored by green fluorescence in Ch02, whereas brightfield and side-scattered images were obtained in Ch01 and Ch06. The fraction of transfected cells increased from 2.4% at 20 h to 8.5% at the end of 28 h indicating the significant number of transfected cells appearing after 28 h. A gradual release of RBP from core-shell nanofibers, its uptake, and the event of suicide gene expression by transfected cells account for the delayed GFP expression monitored after 20 h. After 48 h, GFP/CD::UPRT suicide gene expression increased to 17% which is sufficient to convert prodrug 5-FC into toxic metabolites such as 5-FUMP, 5-FdUMP, and 5-FUTP in order to foster host cell apoptosis (expressing suicide gene) and subsequent bystander effects. As observed in the release study, almost 85% of RBP polyplexes were released by the end of 32 h; the percent of transfected cell population plateaued at 17% by the end of 48 h. The time span of CD::UPRT gene delivery, transfection, and expression (i.e., nearly 32 h) clearly suggests that suicide gene's antiproliferative effects against A549 cells will be effectively observed only after 32 h. On the basis of these observations, CD::UPRT suicide gene therapy efficacy was monitored at 48 and 96 h by cell viability assay.

3.7. Bystander Effects of CD::UPRT Suicide Gene Therapy.

Apart from inducing apoptosis in the host cell, the antiproliferative metabolites transduced by CD::UPRT enzyme also act upon the cells in the vicinity, thereby mediating the bystander effects. A combination of dyes Hoechst 33342 and PI was used to observe the bystander effects under a fluorescence microscope. The live cell nucleus was stained with Hoechst 33342, whereas the dead cell nucleus was stained with PI alone. The transfected cells expressed GFP which makes them distinctly visible under green filter. In the initial stages (i.e., before 28 h), although transfected cells (GFP/CD::UPRT expressing cells) were observed, no significant number of dead cells (stained with PI) were present (Figure 9a–c). In the later stages, transfected cells expressing CD::UPRT enzyme converted prodrug 5-FC into 5-FU and led to apoptosis of the host cell. Transfected A549 cells expressing CD::UPRT gene underwent apoptosis and were visible under both green filter (GFP expression) and red filter (dead cell nucleus stained with PI) (Figure 9d–f). At the same time point, a few nontransfected dead cells stained with PI were also observed in the vicinity which indicated bystander effects were caused by toxic metabolic intermediates generated by CD::UPRT enzyme (Figure 9g–i). Similar observations were made in FE-SEM imaging of cells, wherein transfected cells underwent membrane blebbing (characteristic event of apoptosis), whereas nearby nontransfected cells retained their native morphology (Figure 10c, d).¹⁷ Thus, a cascade of events taking place in

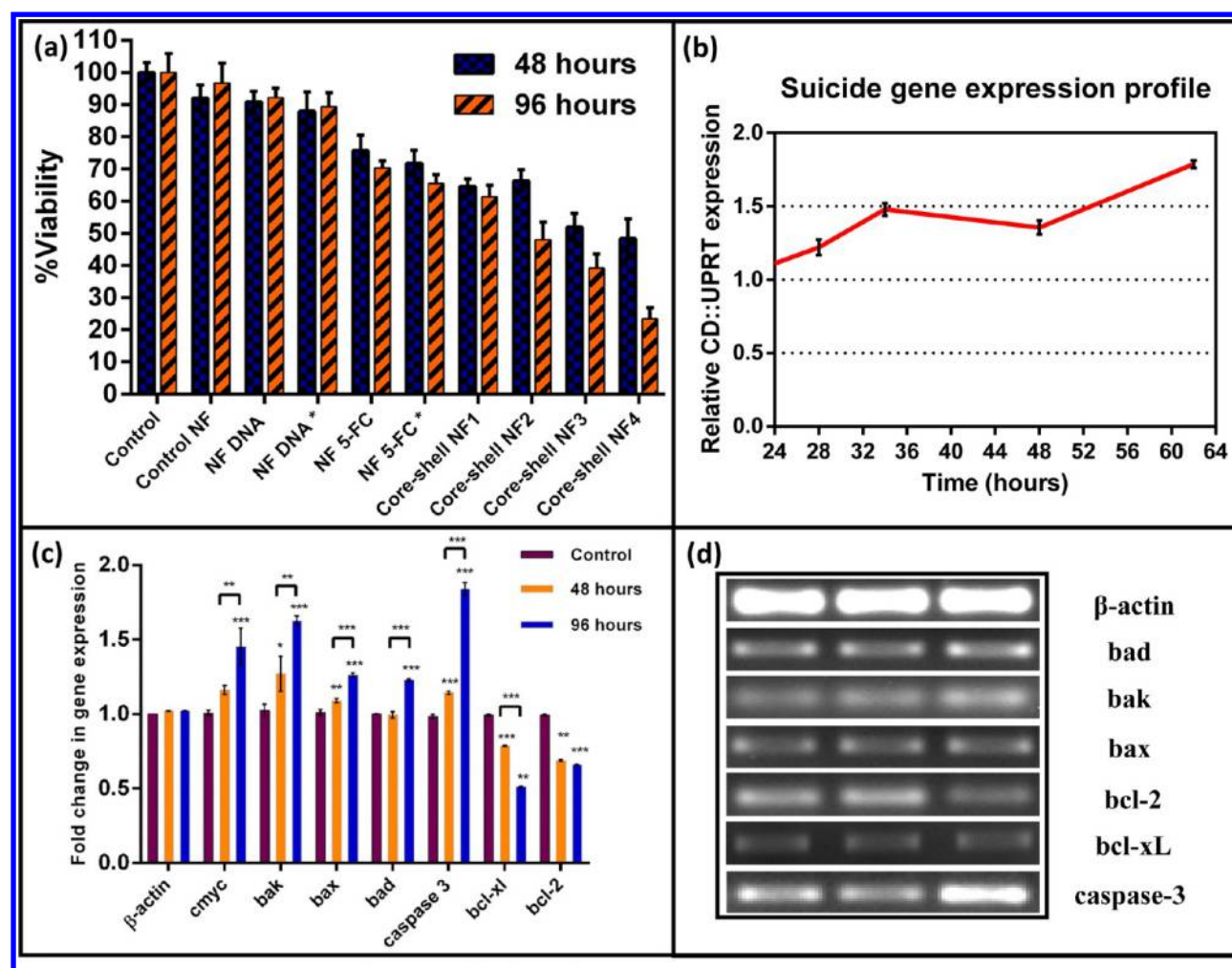


Figure 12. (a) A549 cell viability after 48 and 96 h of seeding over core-shell nanofibers loaded with suicide gene and prodrug, (b) level of CD::UPRT gene expression by transfected A549 cells at different time points, (c, d) relative gene expression profile of apoptotic genes at 48 and 96 h.

CD::UPRT suicide gene therapy commends that higher transfection efficiency is not a prerequisite for attaining effective GDEPT against cancer cells.

3.8. RBP Polyplex Cellular Uptake. The representative images depicting RBP polyplex release from core-shell nanofibers followed by its attachment onto the cell membrane during the initial stages of incubation could be captured effectively by FE-SEM (Figure 10a, b). As evident from FE-SEM images, RBP polyplexes were intact and uniform in morphology even after release from core-shell nanofibers.

3.9. Monitoring Suicide Gene Therapy by Flow Cytometer. A gradual shift in cell population was observed as the suicide gene therapy progressed, which was quantified by a flow cytometer at different time points (Figure 11). The total cell population was classified by flow cytometer as % live or dead cells and % transfected cell or nontransfected A549 cells. The transfected cells expressing GFP were monitored by its green fluorescence in Ch02, whereas nontransfected cells appeared only in Ch01 (brightfield image) alone. The dead cell nucleus stained with PI was distinctly visible in Ch04 when excited by a 488 nm laser. Both GFP and PI were excited by a 488 laser with the power optimized to a value sufficient to detect green fluorescence of transfected cells and at the same time not high enough to saturate PI stained cells. After 24 h, around 3.43% of GFP/CD::UPRT transfected cells were alive

and 1.84% of GFP/CD::UPRT were dead. As compared to the control nanofibers, cell viability was reduced by 13.3% by the end of 24 h in the case of RBP and 5-FC loaded core-shell nanofibers. The cell viability difference arises partly because of GFP/CD::UPRT suicide gene and the rest because of 5-FC and bPEI toxicity. Subsequently at 36 h, the fraction of live transfected cells increased to 6.81% along with a corresponding increase in dead transfected cells (i.e., from 1.84% at 24 h to 3.06% at the end of 36 h). The cell viability was further reduced to 63.41% by the end of 36 h which also included 6.81% of cells expressing GFP/CD::UPRT suicide gene. As an outcome of A549 cells expressing suicide gene (i.e., 6.81% at 36 h), a drastic decline in cell viability was observed at 72 h, that is, 46.11% (39.9% nontransfected live cells and 6.21% transfected live cells). With an increasing time span of incubation, cell population migrates from III quadrant (nontransfected) to IV (dead cells) and II quadrant (transfected cells). Moreover, a few transfected cells which have completely lost the membrane integrity lose GFP proteins too and, thus, could also migrate from quadrant IV to II straightaway instead of staying in quadrant I. Although the percentage of transfected cells was almost the same at 36 and 72 h, there was a significant increase in percentage of dead transfected cells (i.e., from 3.06% to 11.6%) clearly indicating that sustained release of RBP polyplexes and transfection of new A549 cells replenishes the

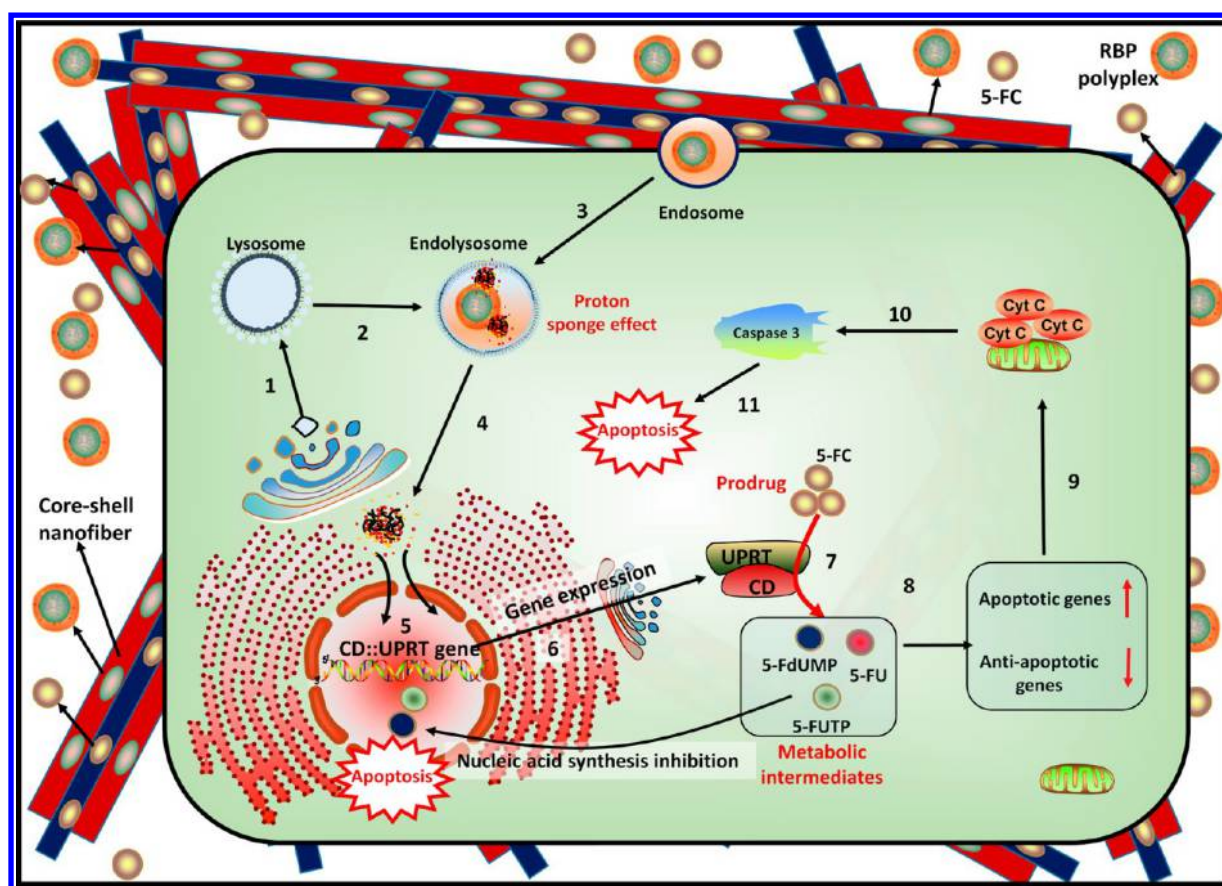


Figure 13. Schematic outline of suicide gene therapy mediated by core-shell nanofibers loaded with RBP polyplexes and 5-FC. Steps 1–7 are common entry pathways for RBP polyplexes followed by steps 8–11 which indicates p53 mediated apoptotic pathway usually followed by most of the anticancer drugs.

dead transfected cells up to 72 h. The core-shell control nanofibers loaded with RBP alone accounted for 16.5% GFP/CD::UPRT suicide gene transfection in A549 cells by the end of 72 h. At the outset, it is these 16.5% of transfected cells that account for almost 34% decline in cell viability. The difference in percent of transfected cells and dead cells (i.e., $34\% - 16.5\% = 17.5\%$) arises solely because of the bystander effects of CD::UPRT.

3.10. Cell Viability Assay. Only a negligible difference in cell viability was observed between core-shell nanofibers loaded with different extents of RBP (0.11 and 0.22 wt %) or 5-FC (0.25 and 0.5 wt %), that is, 1.79% and 3.63%, respectively, by the end of 48 h (Figure 12a). Absence of such cell viability difference at 48 h arises because of delayed transfection of CD::UPRT suicide gene which could effectively mediate antiproliferative effects at later stages only (i.e., after 48 h). Thus, at later stages, that is, at 96 h, the cell viability difference widened further as all transfected A549 cells underwent apoptosis in the presence of prodrug 5-FC and also augmented the bystander effects. As expected, with an increase in concentration of either RBP polyplexes or 5-FC, the cell viability decreased independently. Moreover, different polyplex concentrations could attain higher cell viability differences (i.e., 15.78% between core-shell NF3 and NF4) as compared to those with different 5-FC concentrations (13.39% between core-shell NF1 and NF2). This observation indicates that, although transfection % and 5-FC concentration augment each other in mediating apoptosis, the percent of transfected cells has better influence on cell viability as compared to

concentration of 5-FC. The core-shell NF4 loaded with higher limits of RBP polyplexes and 5-FC (core-shell NF4) could manifest the lowest cell viability at 96 h.

3.11. Gene Expression Studies. Semiquantitative RT-PCR analysis of RNA isolated from treated A549 cells at different time points confirmed genomic integration and expression of CD::UPRT suicide gene. With passage of time, expression of suicide gene gradually increases indicating greater fraction of transfected cells (Figure 12b). Apart from suicide gene expression, relative expression of apoptotic genes was also quantified for treated A549 cells at 48 and 96 h. As observed in cell viability assay, no significant difference in expression of pro-apoptotic or antiapoptotic gene expression was observed until 48 h, whereas at 96 h significant up-regulation of apoptotic genes and consequent down-regulation of antiapoptotic genes was observed (Figure 12c, d). Apoptotic genes *c-myc*, *bak*, and *caspase 3* expressions were up-regulated very prominently as compared to the rest, which is clearly indicative of apoptosis. Pre-existing literature also supports CD::UPRT/5-FC mediated up-regulation of pro-apoptotic genes as observed in this work.¹⁸ The translated products of *bax*, *bad*, and *bak* genes generate oligomeric pores in the outer membrane of mitochondria as an outcome of which cytochrome *c* present within mitochondria is released. The cytochrome *c* present in the cytosol further activates the caspase family of genes leading to nuclear genome fragmentation which is the characteristic feature of cells undergoing apoptosis.¹⁹ Activation of apoptotic gene cascade instigates interplay of multiple pathways which ultimately culminates in apoptosis.²⁰

4. CONCLUSION

The core-shell nanofibrous scaffold fabricated in this work has been validated to attain independent delivery of both suicide gene and prodrug in a controlled and sustained manner over a prolonged time span. In the initial stages, RhoB tagged RBP polyplexes present in the nanofiber shell were released, leading to transfection and expression of suicide gene CD::UPRT in A549 cells (Figure 13). Henceforth, gradual increase in A549 cells expressing GFP/CD::UPRT gene was monitored with the passage of time. The prodrug (5-FC) loaded in the nanofiber core was subsequently released which was later transformed into toxic metabolites (5-FU, 5-FUMP, 5-FdUMP, 5-FUTP) when acted upon by CD::UPRT enzyme expressed by transfected A549 cells. The time lag attained between delivery of RBP polyplexes and prodrug 5-FC also favors improved therapeutic efficacy. Apart from inducing apoptosis in transfected A549 cells, CD::UPRT suicide gene could also effectively mediate bystander effects to cells in the vicinity which further augments therapeutic efficacy of suicide gene therapy. Moreover, time-dependent antiproliferative effects of suicide gene therapy were ascertained on qualitative and quantitative basis by various staining procedures and assays. Such versatile core-shell nanofiber scaffold for subsequent delivery of suicide gene and prodrug has been attained for the first time, and thus, this work opens up new application for an ever expanding field of nanofibrous scaffolds.

■ ASSOCIATED CONTENT

Supporting Information

The Supporting Information is available free of charge on the ACS Publications website at DOI: 10.1021/acsami.5b05280.

Gene-specific primers used for apoptotic gene expression studies, DNase I protection assay, and schematic representation of glutaraldehyde mediated cross-linking reaction (PDF)

■ AUTHOR INFORMATION

Corresponding Author

*Tel: +91-1332-285650. Fax: +91-1332-273560. E-mail: pgopifnt@iitr.ernet.in; genegopi@gmail.com.

Notes

The authors declare no competing financial interest.

■ ACKNOWLEDGMENTS

This work was supported by the Science and Engineering Research Board (No. SR/FT/LS-57/2012), Department of Biotechnology (No. BT/PR6804/GBD/27/486/2012), and Ministry of Human Resource Development (Faculty initiation grant, IIT Roorkee), Government of India. S.U.K. is thankful to the Ministry of Human Resource Development, Government of India, for the fellowship. Sincere thanks to Department of Chemistry and Institute Instrumentation Centre, IIT Roorkee, for the various analytical facilities provided.

■ REFERENCES

- (1) Lee, S.; Jin, G.; Jang, J. H. Electrospun Nanofibers as Versatile Interfaces for Efficient Gene Delivery. *J. Biol. Eng.* **2014**, *8*, 30–34.
- (2) Vasita, R.; Katti, D. S. Nanofibers and their Applications in Tissue Engineering. *Int. J. Nanomedicine* **2006**, *1* (1), 15–30.
- (3) Alekseenko, I. V.; Snezhkov, E. V.; Chernov, I. P.; Pleshkan, V. V.; Potapov, V. K.; Sass, A. V.; Monastyrskaya, G. S.; Kopantzev, E. P.; Vinogradova, T. V.; Khramtsov, Y. V.; Ulasov, A. V.; Rosenkranz, A.

A.; Sobolev, A. S.; Bezborodova, O. A.; Plyutinskaya, A. D.; Nemtsova, E. R.; Yakubovskaya, R. I.; Sverdlov, E. D. Therapeutic Properties of a Vector Carrying the HSV Thymidine Kinase and GM-CSF Genes and Delivered as a Complex with a Cationic Copolymer. *J. Transl. Med.* **2015**, *13* (1), 78.

(4) Duarte, S.; Carle, G.; Faneca, H.; de Lima, M. C.; Pierrefite-Carle, V. Suicide Gene Therapy in Cancer: Where Do We Stand Now? *Cancer Lett.* **2012**, *324* (2), 160–170.

(5) Gopinath, P.; Ghosh, S. S. Implication of Functional Activity for Determining Therapeutic Efficacy of Suicide Genes In Vitro. *Biotechnol. Lett.* **2008**, *30* (11), 1913–1921.

(6) Kucerova, L.; Altanerova, V.; Matuskova, M.; Tyciakova, S.; Altaner, C. Adipose Tissue-Derived Human Mesenchymal Stem Cells Mediated Prodrug Cancer Gene Therapy. *Cancer Res.* **2007**, *67* (13), 6304–13.

(7) Altaner, C.; Altanerova, V.; Cihova, M.; Ondicova, K.; Rychly, B.; Baciak, L.; Mravec, B. Complete Regression of Glioblastoma by Mesenchymal Stem Cells Mediated Prodrug Gene Therapy Simulating Clinical Therapeutic Scenario. *Int. J. Cancer* **2014**, *134* (6), 1458–1465.

(8) Hsu, C. Y.; Uludag, H. A Simple and Rapid Nonviral Approach to Efficiently Transfect Primary Tissue-derived Cells Using Polyethylenimine. *Nat. Protoc.* **2012**, *7* (5), 935–45.

(9) Benjaminsen, V. R.; Mattheijberg, M. A.; Henriksen, J. R.; Moghimi, S. M.; Andresen, T. L. The Possible “Proton Sponge” Effect of Polyethylenimine (PEI) Does Not Include Change in Lysosomal pH. *Mol. Ther.* **2013**, *21* (1), 149–157.

(10) Kumar, S. U.; Gopinath, P. Controlled Delivery of bPEI-Niclosamide Complexes by PEO Nanofibers and Evaluation of its Anti-Neoplastic Potentials. *Colloids Surf., B* **2015**, *131*, 170–181.

(11) Lambert, J. B. *Introduction to Organic Spectroscopy*; Macmillan: New York, 1987; ISBN 0023673001.

(12) Shen, S. L.; Chen, X. P.; Zhang, X. F.; Miao, J. Y.; Zhao, B. X. A Rhodamine Based Lysosomal pH Probe. *J. Mater. Chem. B* **2015**, *3*, 919–924.

(13) Denny, W. A. Prodrugs for Gene-Directed Enzyme-Prodrug Therapy (Suicide Gene Therapy). *J. Biomed Biotechnol.* **2003**, *1*, 48–70.

(14) Kumar, S. U.; Matai, I.; Dubey, P.; Bhushan, B.; Sachdev, A.; Gopinath, P. Differentially Cross-Linkable Core-Shell Nanofibers for Tunable Delivery of Anticancer Drugs: Synthesis, Characterization and their Anticancer Efficacy. *RSC Adv.* **2014**, *4*, 38263.

(15) Blau, A. Cell Adhesion Promotion Strategies for Signal Transduction Enhancement in Microelectrode Array In Vitro Electrophysiology: An Introductory Overview and Critical Discussion. *Curr. Opin. Colloid Interface Sci.* **2013**, *18* (5), 481–492.

(16) Lee, C. H.; Ni, Y. H.; Chen, C. C.; Chou, C. K.; Chang, F. H. Synergistic Effect of Polyethylenimine and Cationic Liposomes in Nucleic Acid Delivery to Human Cancer Cells. *Biochim. Biophys. Acta, Biomembr.* **2003**, *1611* (1–2), 55–62.

(17) Coleman, M. L.; Sahai, E. A.; Yeo, M.; Bosch, M.; Dewar, A.; Olson, M. F. Membrane Blebbing during Apoptosis Results from Caspase-Mediated Activation of ROCK I. *Nat. Cell Biol.* **2001**, *3* (4), 339–345.

(18) Gopinath, P.; Ghosh, S. S. Apoptotic Induction with Bifunctional E. Coli Cytosine Deaminase-Uracil Phosphoribosyltransferase Mediated Suicide Gene Therapy is Synergized by Curcumin Treatment In Vitro. *Mol. Biotechnol.* **2008**, *39* (1), 39–48.

(19) Aluvila, S.; Mandal, T.; Hustedt, E.; Fajer, P.; Choe, J. Y.; Oh, K. J. Organization of the Mitochondrial Apoptotic BAK Pore: Oligomerization of the BAK Homodimers. *J. Biol. Chem.* **2014**, *289* (5), 2537–2551.

(20) Gopinath, P.; Ghosh, S. S. Understanding Apoptotic Signaling Pathways in Cytosine Deaminase-Uracil Phosphoribosyl Transferase-Mediated Suicide Gene Therapy In Vitro. *Mol. Cell. Biochem.* **2009**, *324* (1–2), 21–29.

Self-Assembled Hybrids of Fluorescent Carbon Dots and PAMAM Dendrimers for Epirubicin Delivery and Intracellular Imaging

Ishita Matai,[†] Abhay Sachdev,[†] and P. Gopinath^{*,†,‡}

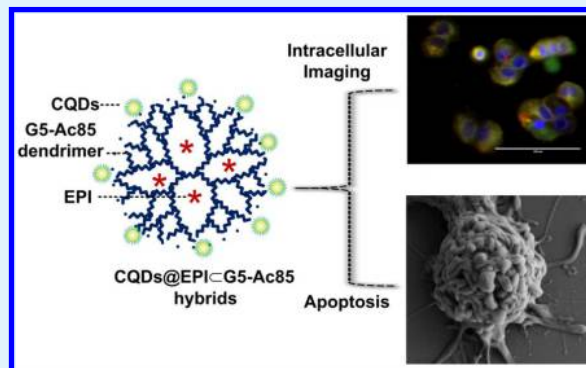
[†]Nanobiotechnology Laboratory, Centre for Nanotechnology, Indian Institute of Technology Roorkee, Roorkee, Uttarakhand-247667, India

[‡]Department of Biotechnology, Indian Institute of Technology Roorkee, Roorkee, Uttarakhand-247667, India

S Supporting Information

ABSTRACT: Advanced nanomaterials integrating imaging and therapeutic modalities on a single platform offers a new horizon in current cancer treatment strategies. Recently, carbon dots (CQDs) have been successfully employed for bioimaging of cancer cells. In the present study, luminescent CQDs with anionic terminus and cationic acetylated G5 poly(amido amine) (G5-Ac85) dendrimers were combined via noncovalent interactions to form self-assembled fluorescent hybrids. The fluorescence of CQDs in hybrids is enhanced in the vicinity of primary amine groups of dendrimers, making them suitable as cellular imaging probes. Encapsulation of chemo-drug epirubicin (EPI) in the dendrimer interiors endowed the fluorescent hybrids with therapeutic potential. The *in vitro* release of an entrapped EPI drug from CQDs@EPI-G5-Ac85 hybrids was faster in an acidic environment than under physiological conditions. Herein, multifunctional CQDs@EPI-G5-Ac85 hybrids serve as a dual-emission delivery system, to track the intracellular distribution and cytotoxic effects of EPI drugs. Green emission properties of CQDs were used for fluorescence microscopic imaging and cellular uptake by flow cytometry. Cell cycle analysis, field-emission scanning electron microscopy (FE-SEM), reactive oxygen species (ROS) generation, and up-regulation of apoptotic signaling genes unanimously demonstrated the apoptosis inducing ability of CQDs@EPI-G5-Ac85 hybrids in breast cancer (MCF-7) cells. Therefore, we have evaluated CQDs@EPI-G5-Ac85 hybrids as prospective candidates to achieve simultaneous imaging and drug delivery in cancer cells.

KEYWORDS: carbon dots, bioimaging, dendrimers, hybrids, epirubicin, drug delivery



1. INTRODUCTION

With the progress in medical nanotechnology, the demand for multifunctional theranostic nanomaterials to combine the therapeutic and imaging modalities into a single agent has increased.¹ Such advanced nanomaterials are expected to bridge the gap between therapy and imaging for concurrent monitoring of therapy response.² Polymer based nanoplateforms such as dendrimers hold great promise for construction of such multifunctional vehicles.^{3,4} Well-defined size, three-dimensional architecture, high density of peripheral functional groups, and a multivalent exterior for multiple conjugation reactions makes dendrimers attractive candidates for drug delivery and molecular imaging.^{5–7} The unique dendritic architecture resolves the traditional drug delivery problems by enhancing the water solubility and bioavailability of hydrophobic drugs.⁸ Among the promising dendritic systems, full generation poly(amido amine) (PAMAM) dendrimers bearing terminal amines have been employed for delivering water-insoluble drugs,^{9,10} anticancer agents,^{11–14} and oligonucleotides for enhanced gene transfection.^{15–18}

Besides delivery, high generation dendrimers have been utilized as a template or stabilizer for metal nanoparticle

synthesis.¹⁹ In our previous work, we have demonstrated the use of G5.0 PAMAM dendrimers as stabilizers for forming amine terminated silver nanoparticles (DsAgNPs) and a carrier of anticancer drug 5-fluorouracil (5-FU). Such a multi-component dendritic system could synergistically induce cell death in breast and lung cancer cells.²⁰ However, amine terminated PAMAM dendrimers are known to suffer from concentration and generation dependent toxicity. Byrne and co-workers correlated the cytotoxic response of PAMAM dendrimers (G4, G5, and G6) with the generation and hence increasing number of surface amine groups using different *in vitro* and *in vivo* models. The cytotoxicity of PAMAM dendrimers was determined by various biological assays whereby G6 > G5 > G4.^{21–24} Hong and group investigated the amine-terminated PAMAM dendrimer interactions with the DMPC (1,2-dimyristoyl-*sn*-glycero-3-phosphocholine) lipid bilayers as well as KB and Rat2 cell membranes. They noted that while high generation G7 PAMAM dendrimers (10–100

Received: March 9, 2015

Accepted: May 6, 2015

nM) caused the formation of nanoscale holes, but G5 PAMAM dendrimers only expanded holes at existing defects.²⁵ The apparent mechanism behind the nanoholes formation could be removal of lipids by dendrimers or direct insertion of dendrimers into the membrane.^{26,27} Thus, the cationic dendritic exterior could be modified to reduce the overall positive charge responsible for its toxicity without compromising its inherent advantages.

Partial surface acetylation or introduction of hydrophilic polymers such as poly(ethylene glycol) (PEG) on the dendrimer periphery can reduce the overall positive charge and hence the cytotoxicity issues of the PAMAM dendrimer.^{28–32} Conversion of primary amines to neutral acetamides is considered a relatively simple methodology with regard to complicated surface conjugation reactions.

Epirubicin (4'-epimer of doxorubicin) belongs to the anthracycline family and is widely used for the treatment of breast, stomach, bladder, lung, and ovarian cancers.³³ Epirubicin (EPI) is known to be better tolerated with reduced cardiotoxicity and comparable antitumor efficacy as doxorubicin.³⁴ However, insufficient EPI delivery (in appropriate concentration) and development of multidrug resistance in cancer cells restrain the achievement of efficient chemotherapy. Incorporation of EPI in polymers such as PAMAM dendrimers can tailor its solubility and hence bioavailability toward cancer cells. The nanosized dendrimer-drug formulations can permeate through the leaky and defective tumor vasculature to accumulate in the tumor region by a well-known enhanced permeability and retention (EPR) effect.^{5,18} Tumors with a poor lymphatic drainage system favor selective accumulation of nanoscale drug delivery systems to exhibit maximal therapeutic benefit with minimal side effects.⁸ The inherent red fluorescence of EPI is advantageous for cell-internalization studies.

Designing strategies for integrating imaging modalities with dendrimers carrying anticancer drugs for concurrent intracellular tracking and therapy offer a new horizon in cancer treatment. Carbon dots (CQDs) with zero dimension are the newest members in the family of luminescent carbon nanomaterials.³⁵ They are highly appreciated for their bright fluorescence, high chemical inertness, high solubility, easy functionalization, and low toxicity compared to conventional dyes and toxic semiconductor quantum dots.^{36,37} These superior features of carbon dots prompt their use in bioimaging applications.^{38–40} Recently, we have synthesized luminescent CQDs through the hydrothermal method and applied them for bioimaging in cancer cells. For this, chitosan was used as the carbonaceous source and poly(ethylene glycol) (PEG) for surface passivation to enhance the fluorescence properties of CQDs. These biocompatible CQDs with bright fluorescence and excellent photostability could label cancer cells with green fluorescence.³⁹

Macromolecules such as PAMAM dendrimers with abundant amine terminal groups can form hybrids with other nanomaterials such as low molecular weight CQDs via molecular self-assembly. CQDs with hydroxyl (–OH) surface groups can noncovalently interact with the cationic acetylated PAMAM dendrimers to form fluorescent hybrids. We intentionally adopted a noncovalent pathway for hybrid formation for its several advantages: (i) a relatively simple approach to a variety of hybrid assemblies, (ii) covalent conjugation by surface modification can quench CQD fluorescence, and (iii) enhancement in CQDs fluorescence by PAMAM dendrimer via charge-

transfer process.^{40,41} Recently, Zhou and co-workers demonstrated use of negatively charged CQDs as caps on positive mesoporous silica nanoparticles (MSPs) for smart delivery of anticancer drug doxorubicin (DOX).⁴² Zong and group reported photoluminescence (PL) enhancement of carbon dots in the vicinity of AuNPs conjugated through G4.0 PAMAM NH₂ dendrimers.⁴³

In the present study, G5 PAMAM dendrimers with larger interiors than G4 dendrimers (~5.4 nm) and lower cytotoxicity than G6 dendrimers were selected for hybrid formation. Herein, self-assembled hybrids of CQDs and EPICG5-Ac85 dendrimer complexes (85 refers to peripheral acetyl groups) as CQDs@EPICG5-Ac85 act as a multifunctional dual-emission and therapeutic system. The emission intensity of CQDs is enhanced after noncovalent complexation with EPICG5-Ac85 complexes. To the best of our knowledge, this is the first instance wherein CQDs have been used to visualize and quantitate the intracellular uptake of EPICG5-Ac85 inclusion complexes by fluorescence microscopy and flow cytometry techniques. CQDs@EPICG5-Ac85 hybrids illustrate pH dependent release of encapsulated EPI drugs and serve as imaging probes in the transport process to their target destination. Various cell based assays were performed to investigate the anticancer activity of EPI in encapsulated form in CQDs@EPICG5-Ac85 hybrids in MCF-7 (breast cancer) and NIH 3T3 (mouse embryonic fibroblast) cells. Further, elucidation of the mode of cell death was done by monitoring the cell cycle distribution, ROS levels by flow cytometry, and differential expression of apoptosis related genes by RT-PCR, respectively. Our results indicated that CQDs@EPICG5-Ac85 hybrids could remarkably reduce the MCF-7 proliferation and induce apoptosis by oxidative DNA disintegration and trigger of mitochondrial pathway of apoptosis. The ability of CQDs@EPICG5-Ac85 hybrids for synchronized bioimaging and drug delivery has been confirmed to achieve improved cancer diagnosis and therapy.

2. EXPERIMENTAL SECTION

Materials. Ethylenediamine core amine-terminated G5 PAMAM dendrimers (M_w 28824.81 g mol⁻¹) with a polydispersity index of less than 1.08 was purchased from Sigma-Aldrich, USA. Acetic anhydride and triethylamine were obtained from Thomas Baker, India. Epirubicin hydrochloride (EPI-HCl) was bought from Sigma-Aldrich, USA. Chitosan and poly(ethylene glycol) (PEG) were purchased from SRL, India. Glacial acetic acid was obtained from SDFCL, India. A regenerated cellulose dialysis membrane (molecular weight cut off, MWCO = 10 kDa) was acquired from Thermo Fisher Scientific, USA. 3-(4,5-Dimethyl-2-thiazoyl)-2,5-diphenyltetrazolium bromide (MTT), 2',7'-dichlorofluorescein diacetate (DCFDA), and 3,8-diamino-5-[3-(diethylmethyllummonio)propyl]-6-phenylphenanthridinium diiodide (PI) were obtained from Sigma-Aldrich, USA. Dulbecco's minimum essential medium (DMEM) and phosphate buffer saline (DPBS; Ca²⁺ and Mg²⁺ free) powders purchased from Sigma-Aldrich, USA were reconstituted prior to use. For all the preparations, ultrapure water (18 MΩ cm) was used.

Surface Acetylation of G5 PAMAM Dendrimers. The ratio between acetic anhydride and the dendrimer was adjusted to convert 70% primary amines on the surface to acetamide groups. The stoichiometric ratio of primary amines/acetic anhydride was kept at 1:1 to achieve the desired extent of surface acetylation.³¹ The typical procedure adopted for the synthesis of partially acetylated PAMAM dendrimers is as follows. G5 PAMAM (31.7 mg, 1.1×10^{-3} mmol) in 10 mL of dry methanol was allowed to react with acetic anhydride (9.4×10^{-3} mL, 9.9×10^{-2} mmol) in the presence of triethylamine (10% molar excess of acetic anhydride) under stirring conditions at room

temperature. Triethylamine was added to quench acetic acid, a side product formed in the reaction. The solution was stirred for 24 h under an argon atmosphere, and methanol was removed under a vacuum to obtain a white colored polymer residue. The polymer residue was redissolved in water and dialyzed against 1 L of PBS followed by water for 3 days using a dialysis membrane (MWCO = 10 kDa). The purified samples were then lyophilized and stored at -20°C . The number of primary amines acetylated was determined by ^1H NMR analysis and was found to be 85 groups.

Encapsulation of EPI within G5-Ac85 Interiors. G5-Ac85 dendrimers (10 mg, 0.3×10^{-3} mmol) were dissolved in 1.5 mL of water. Separately, EPI-HCl with 10 mol equiv of dendrimers was dissolved in 300 μL of methanol and neutralized with 5 μL of triethylamine to generate a water-insoluble EPI solution. The EPI solution was then slowly added to the 1.5 mL of dendrimer aqueous solution and magnetically stirred overnight to allow evaporation of methanol solvent. The EPICG5-Ac85 mixture solution was then centrifuged at 7000 rpm for 10 min to remove the precipitates related to noncomplexed free EPI. The supernatants were analyzed spectrophotometrically at 481 nm using an ultraviolet–visible (UV–vis) spectrometer for indirect determination of EPI encapsulation efficiency. The encapsulation efficiency (EE, %) was calculated as follows:

$$\text{EE (\%)} = \frac{\text{Weight of EPI in G5-Ac(85) dendrimers}}{\text{Weight of EPI fed initially}} \times 100$$

Different concentrations of EPI were used to make the EPI calibration curve. For the data fitting, the least-squares approach was used (the regression equation and correlation coefficient at 481 nm were $y = 0.0135x - 0.0465$ and 0.9985, respectively). The supernatant was lyophilized for 3 days to obtain EPICG5-Ac85 inclusion complexes and kept at -20°C for further study.

Synthesis of Hydroxyl-Functionalized Carbon Dots (CQDs). Fluorescent CQDs were synthesized as previously reported by our team.³⁹ Chitosan was used as the carbonaceous source and PEG-4000 as the passivating agent. Briefly, 400 mg of chitosan was dissolved in 60 mL of water under stirring conditions, followed by the addition of 300 μL of acetic acid to obtain a homogeneous solution. To this, 400 mg of PEG-4000 powder was added and stirred until dissolved. The homogeneous solution was then shifted to the hydrothermal reactor and sealed. The mixture was then heated at 200°C for 8 h under a N_2 atmosphere. Upon cooling, the solution was centrifuged at 9000 rpm for 20 min to separate the insoluble precipitates from the pure CQDs.

Preparation of CQDs@EPICG5-Ac85 Fluorescent Hybrids. The CQDs@EPICG5-Ac85 hybrids were prepared by conjugating hydroxyl terminated CQDs with cationic EPICG5-Ac85 dendrimer complexes. Typically, 50 μL of 1.33 mg mL^{-1} aqueous CQD stock solution was incubated with EPICG5-Ac85 dendrimers with varying concentrations of EPI (0.625, 1.25, 2.5, 5, and 10 μM) under shaking conditions. Finally, the mixture solution was diluted with 250 μL of ultrapure water and left to react for 24 h at room temperature to obtain CQDs@EPICG5-Ac85 fluorescent hybrids. The amount of CQDs in the hybrids was kept fixed, and its final concentration was 0.221 mg mL^{-1} .

In Vitro Release of EPI from CQDs@EPICG5-Ac85 Hybrids. The release of EPI from hybrids was studied under different pH conditions using an acetate buffer (20 mM, pH 5.5) and PBS (20 mM, pH 7.4) at the same time intervals. A total of 2 mL of CQDs@EPICG5-Ac85 hybrid solution was placed equally in two dialysis bags (MWCO 3500 Da), and the receptor compartments were filled with 10 mL of acetate or PBS buffer with mild agitation (70 rpm). After each interval, that is 1, 2, 3, 4, 5, 6, 8, 10, 12, 24, and 48 h, 5 μL of each buffer solution was withdrawn and measured for EPI absorbance by microvolume spectrophotometer. The concentration of EPI was estimated from the dose-absorption curve of EPI. The percentage of EPI released was quantitated as follows:

$$\text{EPI release (\%)} = \frac{\text{EPI released in medium}}{\text{EPI loaded in CD-G5-Ac(85) hybrids}} \times 100$$

Characterization. UV–Visible Spectroscopic Measurements. Absorption measurements were performed using a Lasany LI-2800, UV–vis spectrophotometer.

Fluorescence Measurements. Fluorescence spectra were recorded using a Hitachi F-4600 fluorescence spectrophotometer. Fluorescence lifetime measurements were acquired with a Fluoro Cube Fluorescence Lifetime System (Horiba Jobin Yvon) equipped with a Nano LED (635 nm) source. The decay curves were analyzed with IBH decay analysis v 6.1 software.

Zeta and Dynamic Light Scattering (DLS) Measurements. The zeta potential and hydrodynamic diameter of CQDs@EPICG5-Ac85 hybrids were estimated using Malvern Nano ZS 90, Zetasizer operating at 25°C .

Transmission Electron Microscopy (TEM). The morphology of CQDs@EPICG5-Ac85 fluorescent hybrids was determined by FEI TECHNAI G2 TEM at an operating voltage 200 kV. A total of 10 μL of CQDs@EPICG5-Ac85 hybrids was drop casted onto a carbon coated copper grid and was viewed after negative staining with 2% phosphotungstic acid (PTA).

Nuclear Magnetic Resonance (^1H NMR) Measurements. Samples were dissolved in millimolar concentrations in D_2O solvent, and ^1H NMR spectra were acquired using a Bruker 500 MHz NMR spectrometer.

Cell Culture. MCF-7 (human breast adenocarcinoma) and NIH 3T3 (mouse embryonic fibroblast) cells were obtained from the National Centre for Cell Sciences (NCCS) Pune, India and cultured in a DMEM medium containing 10% (v/v) fetal bovine serum (FBS, Gibco Life Technologies) and 1% (v/v) penicillin–streptomycin (Sigma-Aldrich, USA) and kept at 37°C in a 5% CO_2 incubator. When the cultured cells reached 70–80% confluence, harvesting was done using 0.25% trypsin-EDTA.

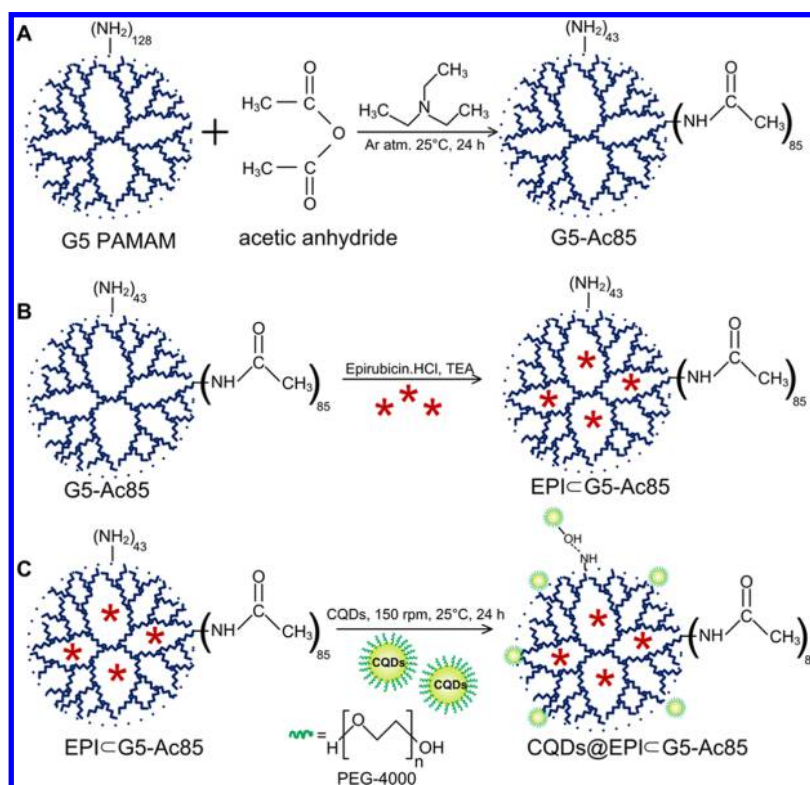
Cytotoxicity Assay. An MTT assay was used to determine the cellular viability. Cells were seeded in a 96-well assay plate at a density of 10 000 cells/well (100 μL total volume/well) for 24 h. Free EPI, EPICG5-Ac85 complexes and CQDs@EPICG5-Ac85 hybrids (with equivalent EPI concentrations) were then added to fresh cell culture medium for 48 h of incubation at 37°C . Free CQDs and G5-Ac85 dendrimers with equivalent mass concentration as in CQDs@EPICG5-Ac85 hybrids were used as controls. Following treatment, a PBS wash was given to remove residual particles. Live cells with active mitochondria can convert the tetrazolium salt to purple formazon crystals. A total of 10 μL of MTT dye was added per well of the assay plate and left for 3 h in 5% CO_2 at 37°C for the appearance of formazon. After 3 h, the medium was aspirated from each well, and 100 μL of DMSO was added to dissolve the formazon product. The absorbance of purple formazon product at 570 nm was quantitated using a microplate reader (Cytation3, Biotek). All of the experiments were performed in triplicate. Cell viability (%) was expressed as

$$\text{Cell Viability (\%)} = \frac{(\text{A570-A690}) \text{ treated cells}}{(\text{A570-A690}) \text{ control cells}} \times 100$$

Intracellular Colocalization Imaging. For cellular imaging, MCF-7 cells (1×10^5 cells/mL) were seeded in 35 mm culture dishes and cultured overnight. Following attachment, free CQDs, free EPI, EPICG5-Ac85, and CQDs@EPICG5-Ac85 hybrids with final EPI concentrations (5 μM) were added to a fresh DMEM medium and left for 12 h of incubation at 37°C . After treatment, cells were washed with PBS twice, and the nucleus was stained with 2 μL of Hoechst 33342 dye (10 mg mL^{-1}) for 10 min. Cells were then analyzed for fluorescent signals using inverted fluorescent microscopy (EVOS FL Color, AMEFC 4300). For imaging, the filters used were DAPI (λ_{ex} 360 nm, λ_{em} 447 nm), GFP (λ_{ex} 470 nm, λ_{em} 525 nm), and RFP (λ_{ex} 530 nm, λ_{em} 593 nm).

Cellular Uptake Studies. Quantitative estimation of cellular uptake of CQDs@EPICG5-Ac85 hybrids was done using a flow cytometer. CQDs exhibit bright green fluorescence with a 488 nm excitation laser in Ch. 02 (505–560 nm), and this enables tracking distribution of hybrids inside the cells. MCF-7 cells (2×10^5 cells/mL) were plated in 35 mm culture dishes and cultured overnight. Subsequently, the

Scheme 1. Schematic Representation of (A) Synthesis of Partially Acetylated G5 PAMAM Dendrimers (G5-Ac85), (B) Encapsulation of Anticancer Drug Epirubicin (EPI) in the Cavities of G5-Ac85 Dendrimers, (C) Synthesis of CQDs@EPICG5-Ac85 Hybrids via Noncovalent Interactions



medium was removed and fresh DMEM medium containing CQDs, EPICG5-Ac85, and CQDs@EPICG5-Ac85 hybrids were added to cells. After 3 h of incubation, cells were washed, trypsinized, and centrifuged at 600g for 6 min. The cell pellet obtained was redispersed in 200 μ L of PBS and analyzed by flow cytometer (Amnis Flowsight). A total of 10 000 events were recorded per sample and analyzed by Amnis Ideas software.

Cell Cycle Analysis. Induction of apoptotic mode of cell death was determined by propidium iodide (PI) staining and subsequent analysis by flow cytometry. MCF-7 cells at a density of 2×10^5 cells/mL were seeded in 35 mm culture plates for overnight attachment. Free CQDs, Free EPI, EPICG5-Ac85, and CQDs@EPICG5-Ac85 hybrids (with final dose of EPI 5 μ M) were then added to fresh cell culture medium. After 48 h of incubation, the medium was carefully removed to prevent a loss of floating cells, washed with PBS, trypsinized, and harvested by centrifugation at 200g for 5 min. Cells were then fixed with 70% alcohol in ice for 15 min. Next, fixed cells were stained with PI staining solution (50 μ g/mL PI, 1 mg/mL RNase A, and 0.05% triton X-100) for 45 min at 37 $^{\circ}$ C in dark. The amount of PI-labeled DNA was then measured from the cell cycle distribution using a flow cytometer (Amnis Flowsight). A total of 10 000 cells was analyzed for fluorescent signals per sample.

Cell Morphology Analysis by FE-SEM. MCF-7 cells were seeded on sterile glass coverslips in 35 mm culture plates and nursed for 24 h. After that, CQDs@EPICG5-Ac85 hybrids were added to the cells and kept for 24 h. Cells without hybrids were cultured in media and used as a control sample. After treatment, the cells were washed with PBS and fixed in 2% glutaraldehyde solution for 10 min followed by ethanol gradient fixation (20%, 40%, 60%, and 80%). The air-dried samples were then gold sputtered and examined by FE-SEM (QUANTA 200-FEG) operating at 10 kV.

Generation of Intracellular Reactive Oxygen Species (ROS). ROS production in MCF-7 and NIH 3T3 cells when exposed to CQDs@EPICG5-Ac85 hybrids was determined by DCFH-DA staining. DCFH-DA is a nonfluorescent dye which can permeate through the

plasma membrane into the cells' interior where it is hydrolyzed to DCFH. In the presence of intracellular ROS, DCFH is oxidized to green fluorescent DCF, which can be quantified. For this assay, cells (2×10^5 cells/mL) were seeded in six-well culture dishes and were grown overnight. Thereafter, cells were exposed to varied concentrations of CQDs@EPICG5-Ac85 hybrids for 12 h, harvested, and washed with PBS. The cell pellet was then redispersed in PBS with 20 μ M DCFH-DA and incubated for 10 min at 37 $^{\circ}$ C in the dark. Immediately after incubation, cells were analyzed for DCF fluorescence using a flow cytometer (Amnis Flowsight). A total of 10 000 events were acquired per sample, and ROS generation was estimated in terms of percentage of cells with DCF (green) fluorescence using Amnis Ideas software.

Semiquantitative RT-PCR Analysis. For gene expression studies, MCF-7 cells were plated in 35 mm culture plates and subsequently treated with Free CQDs, EPICG5-Ac85, and CQDs@EPICG5-Ac85 hybrids (final EPI concentration was 5 μ M) for 48 h. Differential expression of apoptotic signaling genes was determined by reverse transcriptase-polymerase chain reaction (RT-PCR). The housekeeping β -actin gene was used as an internal control. Total RNA was isolated from cells using Trizol (Sigma-Aldrich, USA). After that, cDNA was generated from total denatured RNA (1 μ g) by reverse transcription performed at 42 $^{\circ}$ C for 50 min using Super Script II Reverse Transcriptase (Life Technologies, India) in a total mixture of 20 μ L. The steps include an initial denaturation (94 $^{\circ}$ C for 3 min) followed by PCR cycle of denaturation (94 $^{\circ}$ C for 30 s), annealing (60 $^{\circ}$ C for 30 s), extension (72 $^{\circ}$ C for 1 min), and a final extension (72 $^{\circ}$ C for 10 min). Finally, the PCR products were resolved on a 1.2% agarose gel and visualized by ethidium bromide staining under UV light. The fold difference was calculated using Image lab 4.0 software in the same instrument.

Statistical Analysis. The values are expressed as mean \pm standard error mean (SEM) for all experiments. The data were analyzed via Student's *t* test or via two-way ANOVA, whichever was applicable, using GraphPad Prism 6.0, and statistically significant values are denoted by * ($p < 0.05$), ** ($p < 0.005$), and *** ($p < 0.001$).

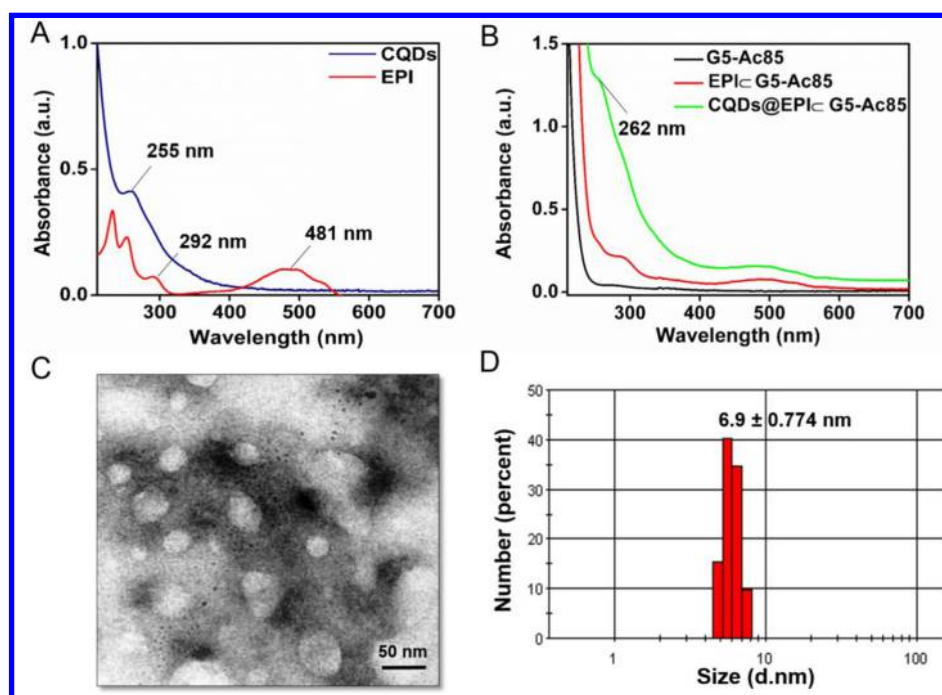


Figure 1. UV–visible spectrum of (A) CQDs in water and EPI in methanol. (B) Aqueous solution of G5-Ac85, EPICG5-Ac85 complexes, and CQDs@EPICG5-Ac85 hybrids. (C) TEM image of as-synthesized CQDs@EPICG5-Ac85 hybrids (with 50 nm scale bar) and (D) size distribution profile by DLS measurements at pH 7.0.

3. RESULTS AND DISCUSSION

Theoretically, the G5 PAMAM dendrimer has 128 primary amine groups on its surface available for modification or functionalization. The chemistry of these terminal groups render a dendrimer with unique properties of water-solubility and reactivity. Exploiting the potential of PAMAM dendrimers as delivery systems while reducing its cytotoxicity is highly appreciable. With this perspective, a fraction of primary amines were converted to neutral acetamide groups, to reduce its toxicity. In this study, the stoichiometric ratio of acetic anhydride/amine groups was kept at 90:1 to achieve 70% conversion of surface amines to acetamides. The ^1H NMR spectra of the acetyl-derivatized G5 PAMAM shows a peak at 1.9 ppm corresponding to $-\text{CH}_3$ protons of the acetyl group (Figure S1). The peaks at 2.2–3.4 ppm can be assigned to the $-\text{CH}_2-$ protons of G5 PAMAM.^{20,31} The number of acetylated primary amines was determined by comparing the intensity of the $-\text{CH}_3$ protons of the acetyl groups to the sum of all $-\text{CH}_2-$ peaks. From NMR integration, the $-\text{CH}_3/-\text{CH}_2-$ ratio was calculated, and 85 primary amine groups were functionalized to acetamides to yield G5-Ac85 dendrimers. The obtained partially acetylated molecules are expected to be more compact and water-soluble, compared to pristine dendrimers due to minimal charge-repulsion from reactive primary amines.³¹

Next, EPI-HCl was neutralized with triethylamine to form water-insoluble EPI to enable its efficient encapsulation within G5-Ac85 hydrophobic interiors. This new formulation of EPICG5-Ac85 complexes is expected to enhance the water solubility and thus bioavailability of EPI. This drug-dendrimer formulation was stored in -20°C and was stable for 1–2 months without any loss in EPI activity. Additionally, hydroxyl ($-\text{OH}$) functionalized carbon dots (CQDs) were synthesized hydrothermally using chitosan as a carbon source and PEG-4000 polymer as the passivating agent. Use of a suitable passivating agent is known to enhance the fluorescence

properties of CQDs.³⁹ CQDs with $-\text{OH}$ overhangs can form hybrids with cationic EPICG5-Ac85 nanocomplexes through noncovalent linkages such as hydrogen-bonding and electrostatic interactions to track the intracellular distribution of EPI. Step-wise representation of synthesis of CQDs@EPICG5-Ac85 hybrids is shown in Scheme 1. Such EPI loaded CQDs@G5-Ac85 hybrids are expected to act as multifunctional dual-emission delivery systems.

The formed CQDs@EPICG5-Ac85 hybrids were characterized by UV–vis spectroscopy. The absorption spectra of aqueous CQDs solution and EPI dissolved in methanol were also recorded for comparison. CQDs display a single absorption band at 255 nm, which can be attributed to $\pi-\pi^*$ transition of the conjugated $\text{C}=\text{C}$ band^{39,44} (Figure 1A). EPI exhibits a characteristic band at 481 nm (Figure 1A). Upon EPI encapsulation, G5-Ac85 complexes exhibit an absorption enhancement at a 481 nm peak when compared to blank G5-Ac85 dendrimers (Figure 1B). This suggests complete entrapment of EPI within the G5-Ac85 interiors. The amount of EPI payload in G5-Ac85 dendrimers was determined from the dose-absorption curve of EPI, and encapsulation efficiency was calculated as $57.36 \pm 1.5\%$. With the formation of CQDs@EPICG5-Ac85 hybrids, the absorption band of CQDs was slightly red-shifted to 262 nm, suggesting interaction between the terminal amines and $-\text{OH}$ groups of CQDs.

Additionally, the zeta potential (ζ) measurements were also recorded to study the surface charge and interactions among various components of nanocomplexes. The zeta potential of CQDs and G5-Ac85 dendrimers was -18.5 and $+16$ mV, respectively. After EPI encapsulation, the zeta of G5-Ac85 dendrimers reduced to $+11.6$ mV, indicating its entrapment within the dendritic architecture. The interactions between the $-\text{COOH}$ groups of EPI and interior tertiary amines of G5-Ac85 dendrimers can be held responsible for the formation of EPICG5-Ac85 complexes. After adding CQDs, the zeta

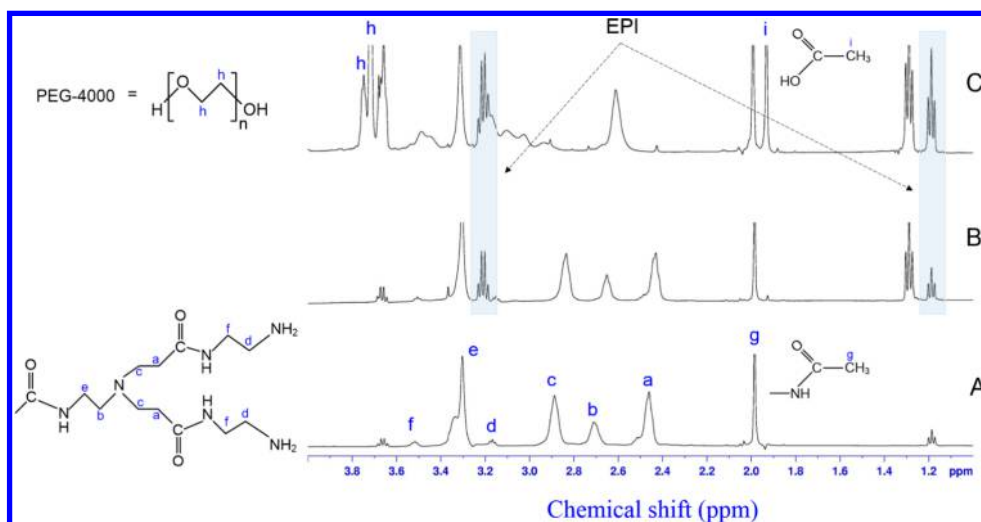


Figure 2. ^1H NMR spectra of (A) G5-Ac85, (B) EPICG5-Ac85 complexes, and (C) CQDs@EPICG5-Ac85 hybrids in D_2O . The highlighted portions (blue) represent the characteristic peaks of EPI.

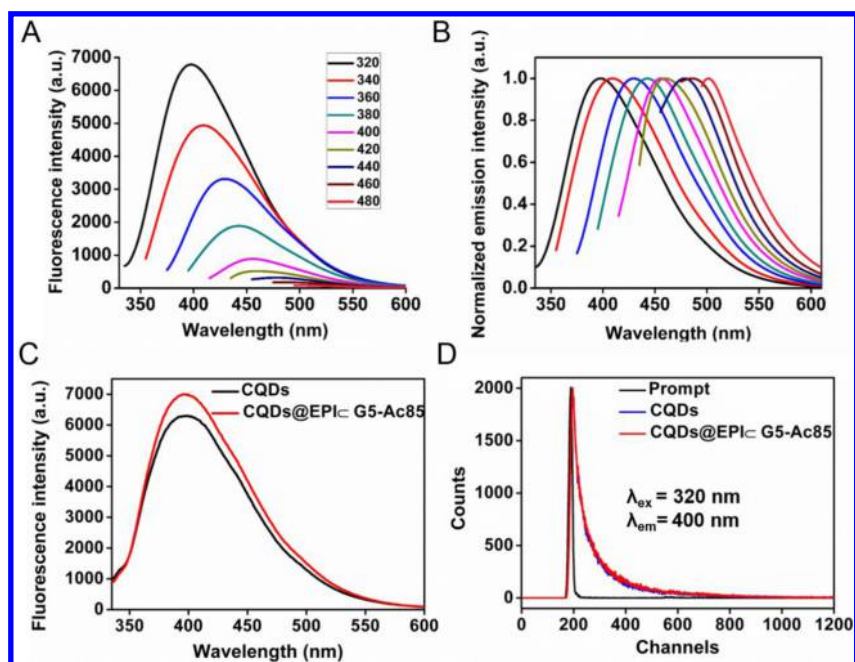


Figure 3. (A) Fluorescence emission spectra of CQDs in water at different excitation wavelengths. (B) Normalized emission spectra. (C) Comparative emission spectra and (D) fluorescence decay profile of CQDs and CQDs@EPICG5-Ac85 hybrids, respectively ($\lambda_{\text{ex}} = 320$ nm; $\lambda_{\text{em}} = 400$ nm).

potential further reduced to +8.74 mV, which indicates efficient grafting of anionic CQDs on the cationic EPICG5-Ac85 surface. The overall positive charge of hybrids makes them suitable candidates for bioapplications such as cellular imaging and for drug delivery.^{44,45}

Further, TEM investigation was done to predict the morphology and size of CQDs and CQDs@EPICG5-Ac85 hybrids. The as-synthesized CQDs appeared nearly spherical with an average size of 1.75 ± 0.474 nm (Figure S2). Negative staining with PTA revealed uniform EPICG5-Ac85 complexes uniformly decorated with CQDs (black spots) to form CQDs@EPICG5-Ac85 hybrids (Figure 1C). DLS measurements showed that the hydrodynamic diameter of as-prepared hybrids was 6.9 ± 0.774 nm (Figure 1D). It is important to mention

that DLS predicts the complete hydrodynamic size of particles.⁴⁶

The formation of EPICG5-Ac85 complexes and CQDs@EPICG5-Ac85 hybrids was further confirmed by ^1H NMR measurements using D_2O as a solvent (Figure 2). TSP (3-(trimethylsilyl) propionic-2,2,3,3- d_4 acid, sodium salt) was used as an internal standard. From Figure 2C, the peak at 1.99 ppm can be assigned to methyl protons of acetamides and peaks at 2.46, 2.71, 2.9, 3.17, 3.32, and 3.52 ppm are representative of the structural protons in an acetylated dendrimer.⁴⁷ With EPI encapsulation (Figure 2B), characteristic peaks of methyl protons of EPI at 1.3 and 3.2 ppm were observed along with acetylated dendrimer proton peaks.⁴⁸ Moreover, for the structural peaks assigned at “b” and “c” positions, a slight upfield shift from 2.71 to 2.65 ppm and 2.9 to

2.8 ppm appeared after EPI complexation, reflecting interaction of EPI molecules with dendrimer secondary amines. The other peaks retained their original positions. With the formation of CQDs@EPICG5-Ac85 hybrids, peaks at ~ 3.7 and 1.93 ppm were seen in conjunction with the other peaks (Figure 2A). These can be attributed to methylene protons of the PEG moiety and remnant acetic acid in CQDs.⁴⁹ The presence of representative NMR peaks of EPI and CQDs indicates the successful formation of EPICG5-Ac85 complexes and CQDs@EPICG5-Ac85 hybrids.

The aqueous solution of CQDs displays the molecular signature excitation dependent emission behavior³⁹ (Figure 3A). Incrementing excitation wavelength from 320 to 480 nm resulted in a progressive red shift in its maximum emission from 400 to 490 nm, with a reduction in emission intensity. The maximum emission of CQDs was recorded at an excitation wavelength of 320 nm. It is worth mentioning that CQDs at 480 nm excitation have negligible emission, resulting in minimal interference with the EPI emission signal. Interestingly, an enhancement in fluorescence of CQDs in CQDs@EPICG5-Ac85 hybrids was encountered compared to blank CQDs (Figure 3C). This can be ascribed to the electron charge transfer from G5-Ac85 dendrimers to CQDs.^{43,50} To confirm this, the fluorescence lifetime decay curves for CQDs and CQDs@EPICG5-Ac85 hybrids were recorded. The obtained data could be fitted to a triple-exponential decay curve, and their average lifetimes were calculated (Figure 3D and Table S1). The average fluorescence lifetime of bare CQDs was 5.84 ns, which increased to 6.12 ns in CQDs@EPICG5-Ac85 hybrids. Thus, grafting of negatively charged CQDs on the PAMAM surface could be a simple and effective strategy for fluorescence enhancement of CQDs.

The effect of change in pH on fluorescence properties of CQDs and CQDs@EPICG5-Ac85 hybrids was also investigated. The emission intensity of both bare CQDs and CQDs@EPICG5-Ac85 hybrids varied with a change in pH of the medium (Figure S3). The fluorescence intensity of CQDs increased steadily in the pH range of 4.0–10.0. However, a slight red shift in emission was monitored from pH 7.0 onward (Figure S3A). With an increase in pH, the terminal $-\text{OH}$ groups of CQDs get ionized which influence electronic transitions resulting in such pH dependent behavior. Contrarily, for CQDs@EPICG5-Ac85 hybrids, maximum fluorescence was evident in an acidic environment (pH 5.5) followed by neutral and alkaline conditions (pH 7.0–10.0; Figure S3B). This can be attributed to the protonation of surface amino groups of PAMAM under acidic conditions and deprotonation under alkaline conditions.^{39,51,52} Their colloidal stability of bare CQDs and CQDs@EPICG5-Ac85 hybrids was also affected with variation in pH (Figure S4). The zeta potential of CQDs was at a maximum of -21.64 mV at pH 10.0 but reduced to -18.5 mV at pH 7.0 and became low under acidic conditions. Conversely, CQDs@EPICG5-Ac85 hybrids were found to exhibit maximum stability at pH 5.5 with a zeta potential of $+28.9$ mV. The pH dependent stability estimations of CQDs and CQDs@EPICG5-Ac85 hybrids are in agreement with the fluorescence results.

Another important parameter is the ability of CQDs@EPICG5-Ac85 hybrids to release the EPI payload in a sustained manner. Before evaluating the anticancer activity, the pH controlled release of EPI by CQDs@EPICG5-Ac85 hybrids was investigated *in vitro* at pH 5.5 and 7.4, respectively. The time-dependent release profiles of EPI are shown in Figure 4.

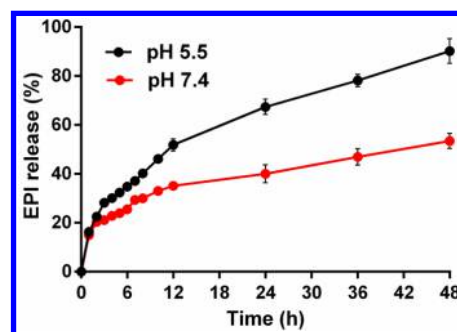


Figure 4. Time-dependent *in vitro* release profiles of EPI (in %) from CQDs@EPICG5-Ac85 hybrids over 48 h in an acetate buffer (pH 5.5, black) and in phosphate buffered saline (pH 7.4, red), respectively.

These hybrids were able to release EPI in a biphasic pattern, characterized by an initial rapid release followed by sustained release. About 90% of EPI was released after 48 h at pH 5.5, imitating the tumor microenvironment. However, around 51% was released in the same time at pH 7.4, close to physiological conditions. The rapid EPI release under acid conditions may be due to weakened electrostatic interactions between protonated interior amines and $-\text{CONH}-$ linkages of CQDs@G5-Ac85 hybrids with $-\text{COOH}$ groups of EPI molecules.⁵¹ The slow release of EPI from CQDs@G5-Ac85 hybrids at physiological pH compared to that under an acidic environment makes it a suitable candidate for specifically targeting the cancerous cells.

We further investigated the anticancer effects of released EPI from EPICG5-Ac85 complexes and CQDs@EPICG5-Ac85 hybrids *in vitro*. As shown in Figure 5A, MCF-7 cells treated with blank G5-Ac85 dendrimers exhibited a good cell viability at all tested concentrations. This suggests that the introduction of a small acetyl moiety on the dendrimer peripheral surface could improve its cytocompatibility. Free CQDs were also able to maintain appreciable cell viability. Free EPI was found to significantly inhibit the cell growth at all studied doses. With an increase in EPI concentration from 0.625 to 10 μM , the cell viability reduced to nearly 16%. Importantly, CQDs@EPICG5-Ac85 hybrids and EPICG5-Ac85 complexes were also able to inhibit cancer cell proliferation significantly. For instance, at an EPI concentration of 5 μM , around 85% of cells died with free EPI and almost 70% cells died with CQDs@EPICG5-Ac85 and EPICG5-Ac85 treatments. Since G5-Ac85 dendrimers did not alter the cell survival, the toxicity was solely induced by the loaded EPI drug. Also, the addition of CQDs to EPICG5-Ac85 complexes did not affect significantly the exhibited toxic response. We also examined the effect of CQDs@EPICG5-Ac85 hybrids on normal NIH 3T3 cells. At a similar dosage, the hybrids exhibited more inhibitory effect on MCF-7 cells compared to normal cells (Figure 5B). Based on the therapeutic profile of EPICG5-Ac85 complexes and CQDs@EPICG5-Ac85 hybrids, 5 μM EPI concentration was selected for further cell-based experiments.

Next, CQDs were examined as fluorescent probes to monitor the intracellular trafficking of CQDs@EPICG5-Ac85 hybrids in MCF-7 cells. Fluorescence microscope imaging is a promising technique to discern the cellular uptake of fluorescent nanomaterials. Figure 6 shows the fluorescence microscopic images of MCF-7 cells incubated with CQDs, EPI, EPICG5-Ac85 complexes, and CQDs@EPICG5-Ac85 hybrids under similar conditions. CQDs appeared intensely green under blue illumination (Figure 6a), and EPI emits red fluorescence under

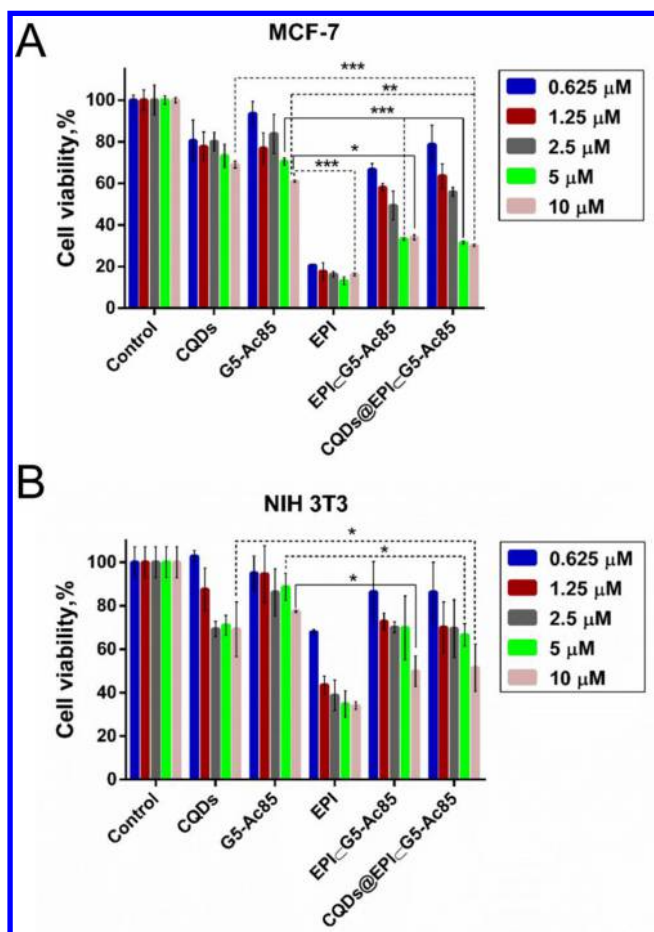


Figure 5. Viability of MCF-7 and NIH 3T3 cells calculated by MTT assay after 48 h of treatment with CQDs, G5-Ac85 dendrimers, EPI, EPICG5-Ac85 complexes, and CQDs@EPICG5-Ac85 hybrids with varying EPI concentrations (0.625, 1.25, 2.5, 5, and 10 μ M). EPICG5-Ac85 complexes, CQDs@EPICG5-Ac85 hybrids, and free EPI had equivalent EPI concentrations. CQDs, G5-Ac85, and CQDs@EPICG5-Ac85 hybrids had equivalent weight concentrations. Experiments were performed in triplicate. Two-way ANOVA with Tukey's multiple comparisons test was used to determine statistical difference between the group means (* p < 0.05, ** p < 0.005, *** p < 0.001).

green light (Figure 6g). Hoechst 33342 dye was used as a fluorescence marker for the nucleus and emitted blue fluorescence under UV light. After 12 h of incubation, CQDs were mostly internalized in the cell cytoplasm but could not enter the nucleus (Figure 6d). This suggests the cytoplasmic region as the main cellular target of free CQDs.^{40,42,46} Interestingly, there was a marked difference in the trafficking of free and encapsulated EPI. Free EPI molecules were mostly localized in the nuclear region as evident from the merged fluorescence image (Figure 6f–h). Probably, free EPI molecules penetrated through the plasma and nuclear membranes to enter the nuclei.⁵³ Conversely, EPICG5-Ac85 complexes were primarily found distributed in the cytoplasmic region (Figure 6j–l). Moreover, CQDs@EPICG5-Ac85 hybrids were also traced in cell cytoplasm surrounding the nucleus and exhibited colocalization of green and red fluorescence (due to release of both CQDs and EPI, respectively; Figure 6m–p). The location of CQDs@G5-Ac85 hybrids in MCF-7 cells after internalization was visualized using lysotracker red, for fluorescence imaging of lysosomes. MCF-7 cells were incubated with CQDs@G5-Ac85 hybrids for 3 h and were then stained with

lysotracker red. After incubation, green fluorescence of hybrids was clearly evident within cells which coincided with the lysotracker red fluorescence (Figure S5). This observation indicated that CQDs@G5-Ac85 hybrids sufficiently accumulated in the cells after internalization and were thereafter transported to lysosomes. These findings suggest lysosomes as the target organelles of CQDs@G5-Ac85 hybrids. The obtained findings demonstrate the significance of luminescent CQDs as fluorescent tracers for cellular delivery of therapeutic agents. Surprisingly, from the fluorescent micrographs, an enhancement in the intensity of the green fluorescent signal of CQDs in CQDs@G5-Ac85 hybrids was monitored. This can be ascribed to the improved delivery and therefore enhanced uptake of CQDs bound to G5-Ac85 dendrimers.

Further, experiments were conducted to quantitate the intracellular uptake of hybrids. For this, MCF-7 cells were incubated with free CQDs, EPICG5-Ac85 complexes, and CQDs@EPICG5-Ac85 hybrids (with an equivalent concentration of CQDs) for 3 h, under the same conditions. After incubation, cells were analyzed using flow cytometry without the use of any other dye. The cellular uptake was measured in terms of percentage of cells expressing green fluorescence (due to uptake of CQDs). The flow cytometric analysis revealed that CQDs were internalized by almost 70% cells compared to cells incubated without CQDs (control). However, about 80% cells could uptake CQDs@EPICG5-Ac85 hybrids under the same parameters (Figure 7A). For EPICG5-Ac85 treated cells, the observed fluorescence (~17%) can primarily be due to the autofluorescent signal of EPI. In a nutshell, both qualitative and quantitative results indicated that G5-Ac85 dendrimers could augment the intracellular distribution and uptake of CQDs. This aspect offers a new horizon in the development of dendrimer based multifunctional vehicles for delivery of imaging and anticancer agents. Although, the exact mechanism of cellular uptake and ultimate cellular fate of nanomaterials in cancer cells is still under investigation. Recent reports suggest clathrin dependent receptor-mediated endocytosis (CME) as the main pathway for internalization of positively charged nanoparticles in MCF-7 cells.^{54–56} For CQDs@EPICG5-Ac85 hybrids carrying an overall positive charge, the probable mechanism of internalization could be classical clathrin-mediated endocytosis.

EPI is known to inhibit the topoisomerase II activity in MCF-7 cells with induction of oxidative DNA damage. Thereafter, cells with failed DNA repair mechanisms, undergo apoptosis.^{57–59} Subsequently, we examined the effect of EPI on the cell cycle and hence DNA damage by PI staining using a flow cytometer. Figure 7B represents the cell cycle distribution pattern of MCF-7 cells incubated with CQDs, EPICG5-Ac85 complexes, and CQDs@EPICG5-Ac85 hybrids (EPI concentration = 5 μ M) for 48 h. The flow cytometric analysis showed that untreated and CQDs treated cells were arrested primarily in the G0/G1 phase. Contrarily, EPICG5-Ac85 complexes or CQDs@EPICG5-Ac85 hybrid treated cells mainly accumulated in the sub G0/G1 phase, i.e., $65.9 \pm 1.41\%$ and $75.7 \pm 0.85\%$, respectively, with respect to untreated cells ($17 \pm 0.42\%$). Moreover, a reduction in the S phase was monitored upon EPI exposure. This implicates DNA damage by EPICG5-Ac85 and CQDs@EPICG5-Ac85 treatment. A substantial increase in the sub G0/G1 phase and reduction in the S phase population is indicative of an apoptotic mode of cell death.^{60,61} After PI staining, CQDs@EPICG5-Ac85 treated cells were examined under FE-SEM to monitor cell morphology alterations. Figure

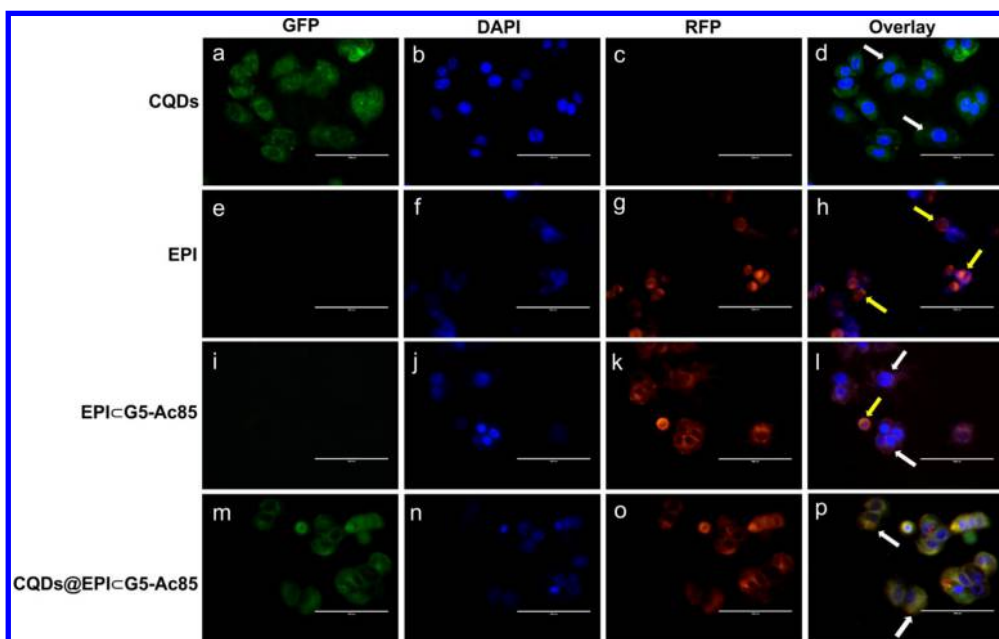


Figure 6. Fluorescence microscope images of MCF-7 cells incubated with free CQDs, free EPI, EPI-G5-Ac85 complexes, and CQDs@EPI-G5-Ac85 hybrids (with equivalent EPI concentration $5 \mu\text{M}$) after 12 h. Intracellular distribution of CQDs is shown in a–d; e–h represent cells treated with EPI; i–l and m–p depicts cells treated with EPI-G5-Ac85 and CQDs@EPI-G5-Ac85 hybrids, respectively. Yellow arrows, nuclear localization; white arrows, cytoplasmic localization (scale bar = $100 \mu\text{m}$).

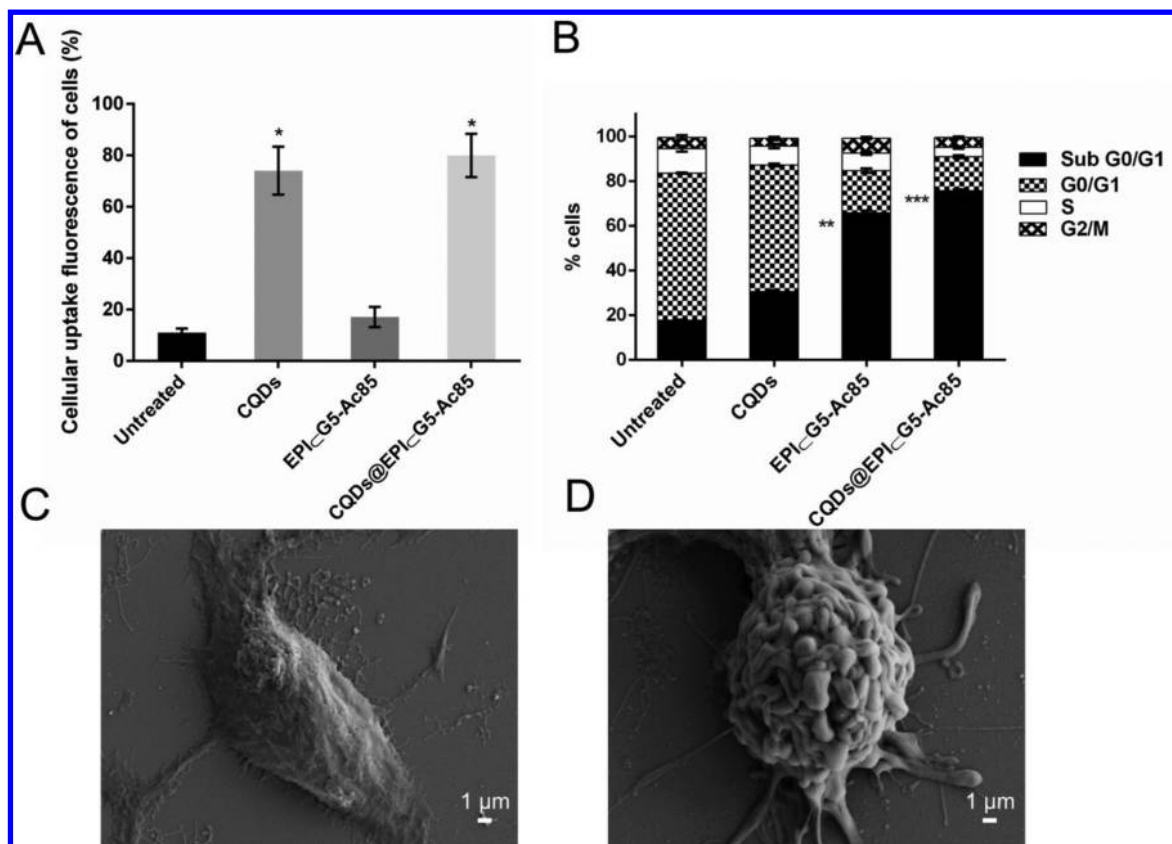


Figure 7. (A) Quantitative cellular uptake in MCF-7 cells after 3 h by flow cytometry. The fluorescence intensity was recorded in channel 02 (505–560 nm). (B) Cell cycle distribution of different samples by flow cytometry. FE-SEM micrographs of (C) untreated and (D) CQDs@EPI-G5-Ac85 hybrids treated MCF-7 cell indicating apoptotic cell death (scale bar = $1 \mu\text{m}$). Statistical significance is denoted by * $p < 0.05$, ** $p < 0.005$, and *** $p < 0.001$.

7C shows the typical morphology of healthy MCF-7 cells. The cells were well adhered to the surface with no signs of

membrane constrictions or damage. However, CQDs@EPI-G5-Ac85 treated cells were round and loosely attached

(Figure 7D). Membrane blebbing and the appearance of apoptotic bodies in treated cells confirm the occurrence of apoptosis.⁶²

Manifestation of free radical generation can result in oxidative stress in cancer cells, causing apoptosis and finally cell death. The ability of free EPI to induce ROS production in breast cancer cells is well documented.⁵⁹ As a proof of concept, we exposed MCF-7 cells to CQDs@EPICG5-Ac85 hybrids with different EPI concentrations for ROS production. The percentage of cells expressing ROS was measured by DCF fluorescence. Figure 8 shows the flow cytometric images of cells with green DCF fluorescence. Each spot in the image reflects the cell expressing ROS. CQDs@EPICG5-Ac85 hybrids were found to induce ROS production in a dose-dependent manner (Figure 8b–e). For instance, CQDs@EPICG5-Ac85 hybrids with 5 μ M EPI could elevate the ROS levels by \sim 86.7% (Figure 8e) with regard to untreated cells (0.61%) (Figure 8a). Such increased cellular oxidative stress can be held responsible for causing DNA damage in cancer cells. It is imperative to mention that fluorescence of CQDs did not interfere during flow measurements owing to its relatively weak signal relative to commercial DCFH-DA dye. Furthermore, we used NIH 3T3 cells to examine the ROS levels in normal cells when exposed to CQDs@EPICG5-Ac85 hybrids. With an increase in the hybrid concentration, the ROS levels in NIH 3T3 cells increased from 5.2% to 13.1%. (Figure S6). However, under similar treatment concentrations, the intracellular ROS production was more in MCF-7 than NIH 3T3 cells. Thus, CQDs@EPICG5-Ac85 hybrids were proficient in inducing apoptosis by causing oxidative stress and, thus, DNA damage in drug resistant breast cancer cells.

To ascertain the molecular signaling pathway involved in CQDs@EPICG5-Ac85 hybrid mediated apoptosis, gene expression analysis was done. Semiquantitative RT-PCR was utilized to validate the expression levels of apoptotic (p53, bax, bad, caspase 3, and c-myc) and antiapoptotic (bcl-xl) genes, respectively. Figure 9A shows the RT-PCR analysis of apoptosis related genes and the computed fold change (Figure 9B). Elevated mRNA expressions of p53, bax, bad, and caspase-3 were observed with down regulation of c-myc and bcl-xl mRNA levels in EPI, EPICG5-Ac85, and CQDs@EPICG5-Ac85 treated samples compared to untreated/CQDs treated cells. The expression of β -actin remained unaltered. A schematic illustration of the apoptotic events involved in CQDs@EPICG5-Ac85 treatment is depicted in Figure 9C.

Internalization of CQDs@EPICG5-Ac85 hybrids causes membrane destabilization and generation of ROS, which in turn triggers the activation of an intrinsic/mitochondrial apoptosis pathway. EPI treatment results in transcriptional activation of the p53 gene, which is pivotal to promoting apoptosis in tumor cells.^{63,64} After treatment, the p53 mRNA levels significantly enhanced ($p < 0.005$), which indicates turning-on of p53 mediated gene signaling cascade. Bcl-xl (basal cell lymphoma-extra large), a member of the bcl-2 family of proteins, is known to protect cells from undergoing apoptosis. Hence, suppression of the bcl-xl gene is essential for initiation of apoptotic events.⁶⁵ A significant down regulation in the bcl-xl gene ($p < 0.001$) in treated samples marks the onset of apoptosis. The transcription factor p53 further upregulates bax (bcl-2-associated X protein) and bad (bcl-2-associated death promoter) levels, which accelerates apoptosis.⁶⁶ Relocalization of bax from the mitochondrial membrane to cytosol leads to outer membrane permeabiliza-

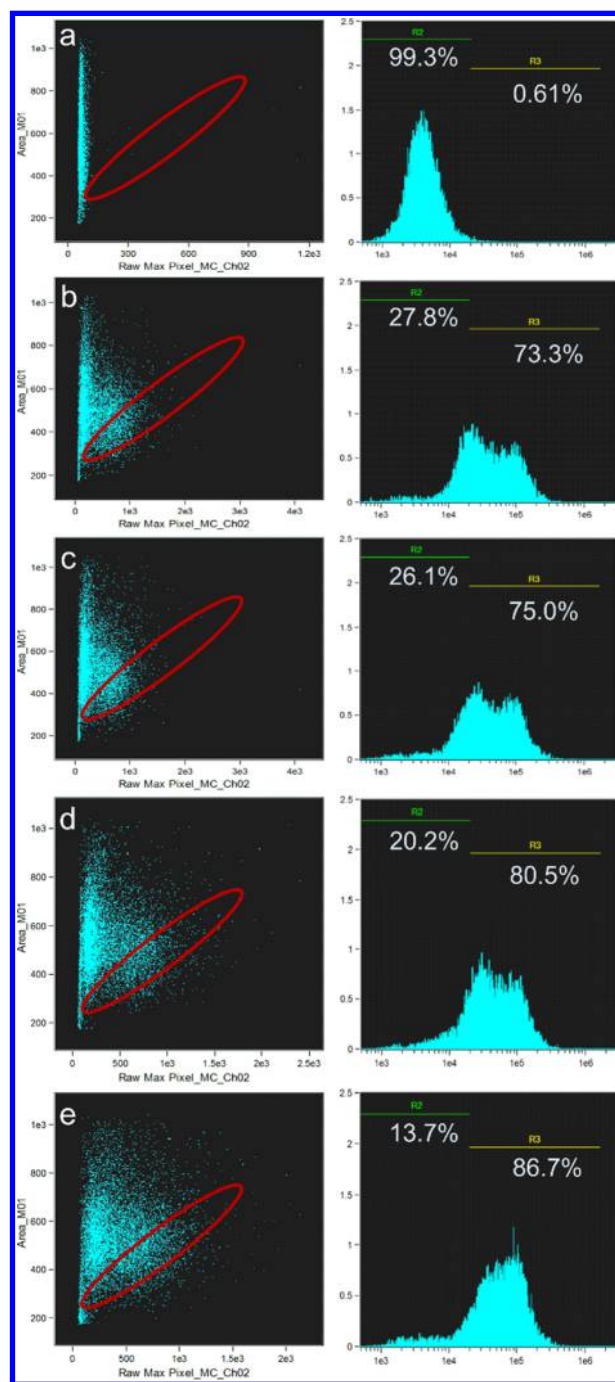


Figure 8. Flow cytometric analysis of ROS production in MCF-7 cells treated with CQDs@EPICG5-Ac85 hybrids with varying concentrations of EPI. Untreated cells are shown in a; b–e depict cells treated with CQDs@EPICG5-Ac85 hybrids with EPI concentrations of 0.625, 1.25, 2.5, and 5 μ M, respectively. Left panel: dot plots of DCF fluorescence. Right panel: corresponding fluorescence histogram.

tion (MOMP) and pore formation to allow cytochrome c (cyt. c) release. The released cyt. c triggers activation of cysteine-aspartic acid proteases (caspase 3) which are the key executioners of apoptosis.⁶⁷ Caspase 3 is identified to induce various biochemical changes and morphological changes in cancer cells.⁶⁸ In EPI treated cells, a significant upregulation of caspase 3 ($p < 0.005$) correlates with the observed DNA damage and formation of apoptotic bodies. Also, EPI is identified to suppress the c-myc mRNA levels.⁶⁹ We also observed

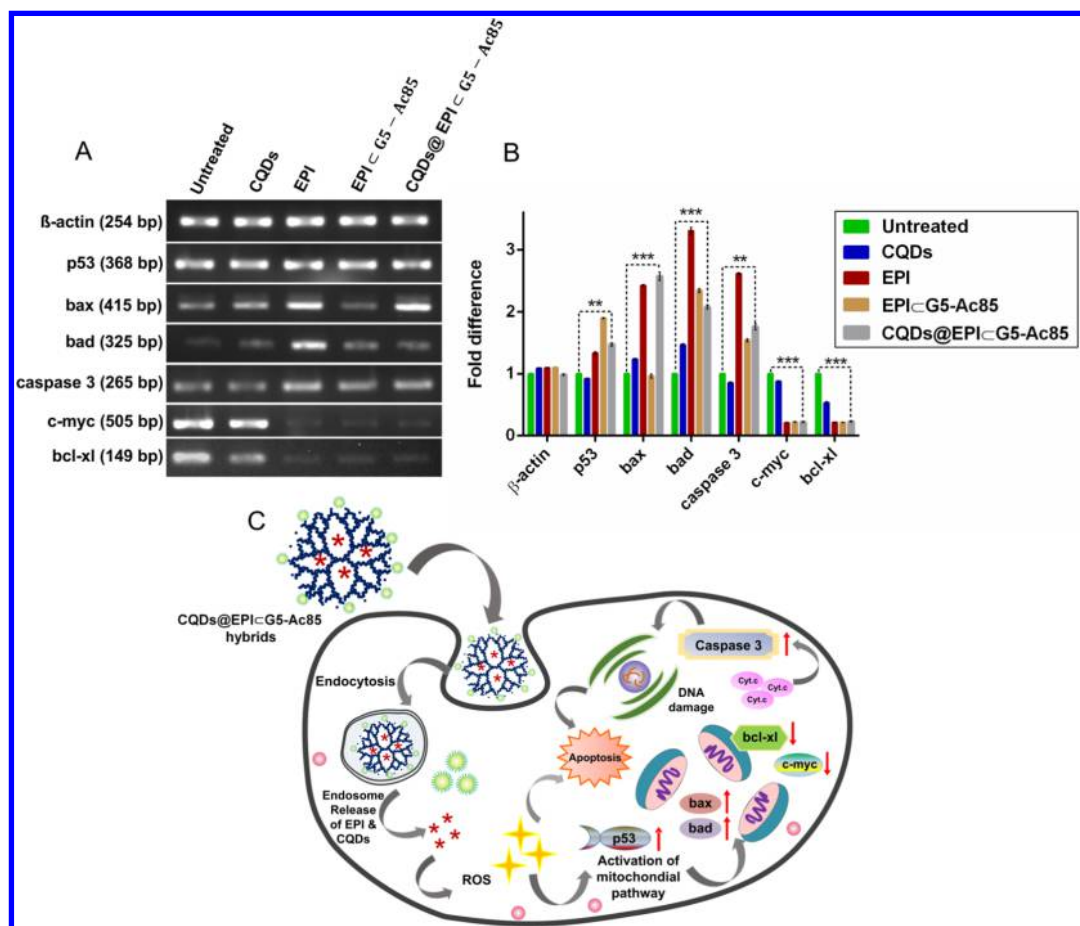


Figure 9. (A) Semiquantitative RT-PCR analysis of apoptotic signaling genes and (B) fold difference in gene expression. Statistical significance between CQDs@EPI@G5-Ac85 treated vs untreated MCF-7 cells is denoted by $**p < 0.005$ and $***p < 0.001$. (C) Schematic illustration of cellular uptake and apoptotic events following CQDs@EPI@G5-Ac85 hybrid treatment.

drastically reduced c-myc mRNA levels, indicating EPI induced toxicity in breast cancer cells. Altogether, our findings strongly suggest that CQDs@EPI@G5-Ac85 hybrids induced apoptosis in breast cancer cells through oxidative DNA damage and trigger p53 mediated gene signaling cascade. Understanding of cellular and molecular mechanisms behind CQDs@EPI@G5-Ac85 mediated cell death can be vital in designing strategies for improved cancer therapy. Moreover, such a complicated regulatory pathway necessitates the development of a multifunctional nanovehicle like G5-Ac dendrimers for real-time delivery of epirubicin and fluorescent probes such as CQDs for improved cancer diagnostics and therapy.

4. CONCLUSION

Herein, we report CQDs@EPI@G5-Ac85 hybrids for monitoring the cellular distribution of anticancer drug epirubicin (EPI) in MCF-7 cells. Hydroxyl-functionalized CQDs could electrostatically interact with cationic acetylated dendrimers to form fluorescent hybrids. Interestingly, an enhancement in CQDs fluorescence and lifetime was witnessed with CQDs@G5-Ac85 hybrid formation. Moreover, CQDs@G5-Ac85 hybrids can function as a dual-emission system, by combining the green fluorescence of CQDs with the EPI red fluorescence. These steps in the practical utility of CQDs@G5-Ac85 hybrids to track the uptake of chemotherapeutic agents. Further, various cell biological assays confirm the applicability of CQDs@EPI@G5-Ac85 hybrids to induce cell death in breast cancer

cells. The rationale behind cell killing involves ROS generation to induce DNA fragmentation and triggering of an intrinsic mitochondrial apoptotic pathway. In a nutshell, the present work prompts the applicability of multifunctional CQDs@EPI@G5-Ac85 hybrids for cancer imaging and therapy. Further studies on functionalization of CQDs@G5-Ac85 hybrids to attain target specificity are underway.

■ ASSOCIATED CONTENT

§ Supporting Information

^1H NMR spectra, TEM images with size distribution data, lifetime data table, emission spectra, zeta potential results, fluorescence microscopic images, and ROS data are included. The Supporting Information is available free of charge on the ACS Publications website at DOI: 10.1021/acsami.5b02095.

■ AUTHOR INFORMATION

Corresponding Author

*Tel.: 91-1332-285650. Fax: +91-1332-273560. E-mail: pgopifnt@iitr.ernet.in. genegopi@gmail.com.

Notes

The authors declare no competing financial interest.

■ ACKNOWLEDGMENTS

We give sincere thanks to the Science and Engineering Research Board (No. SR/FT/LS-57/2012) and Department of Biotechnology (No. BT/PR6804/GBD/27/486/2012),

Government of India, for the financial support. I.M. and A.S. are thankful to the Ministry of Human Resource Development, Government of India, for the fellowship. Department of Chemistry and Institute Instrumentation Centre, Indian Institute of Technology Roorkee are sincerely acknowledged for providing various analytical facilities.

REFERENCES

- (1) Xie, J.; Lee, S.; Chen, X. Nanoparticle-Based Theranostic Agents. *Adv. Drug Delivery Rev.* **2010**, *62*, 1064–1079.
- (2) Janib, S. M.; Moses, A. S.; MacKay, J. A. Imaging and Drug Delivery using Theranostic Nanoparticles. *Adv. Drug Delivery Rev.* **2010**, *62*, 1052–1063.
- (3) Wang, Z.; Niu, G.; Chen, X. Polymeric Materials for Theranostic Applications. *Pharm. Res.* **2014**, *31*, 1358–1376.
- (4) Wang, D.; Lin, B.; Ai, H. Theranostic Nanoparticles for Cancer and Cardiovascular Applications. *Pharm. Res.* **2014**, *31*, 1390–1406.
- (5) Lee, C. C.; MacKay, J. A.; Frechet, J. M. J.; Szoka, F. C. Designing Dendrimers for Biological Applications. *Nat. Biotechnol.* **2005**, *23*, 1517–26.
- (6) Stiriba, S. E.; Frey, H.; Haag, R. Dendritic Polymers in Biomedical Applications: From Potential to Clinical Use in Diagnostics and Therapy. *Angew. Chem., Int. Ed.* **2002**, *41*, 1329–1334.
- (7) Svenson, S.; Tomalia, D. A. Dendrimers in Biomedical Applications—Reflections on the Field. *Adv. Drug Delivery Rev.* **2005**, *57*, 2106–2129.
- (8) Wolinsky, J. B.; Grinstaff, M. W. Therapeutic and Diagnostic Applications of Dendrimers for Cancer Treatment. *Adv. Drug Delivery Rev.* **2008**, *60*, 1037–1055.
- (9) Meijer, E. W.; Jansen, J.; Brabander-van den Berg, E. Encapsulation of Guest Molecules into a Dendritic Box. *Science* **1994**, *266*, 1226–1229.
- (10) Morgan, M. T.; Carnahan, M. A.; Immoos, C. E.; Ribeiro, A. A.; Finkelstein, S.; Lee, S. J.; Grinstaff, M. W. Dendritic Molecular Capsules for Hydrophobic Compounds. *J. Am. Chem. Soc.* **2003**, *125*, 15485–15489.
- (11) Wang, Y.; Guo, R.; Cao, X.; Shen, M.; Shi, X. Encapsulation of 2-Methoxyestradiol within Multifunctional Poly (amidoamine) Dendrimers for Targeted Cancer Therapy. *Biomaterials* **2011**, *32*, 3322–3329.
- (12) Zheng, Y.; Fu, F.; Zhang, M.; Shen, M.; Zhu, M.; Shi, X. Multifunctional Dendrimers Modified with Alpha-Tocopheryl Succinate for Targeted Cancer Therapy. *Med. Chem. Commun.* **2014**, *5*, 879–885.
- (13) Zhu, J.; Shi, X. Dendrimer-Based Nanodevices for Targeted Drug Delivery Applications. *J. Mater. Chem. B* **2013**, *1*, 4199–4211.
- (14) Zhu, J.; Zheng, L.; Wen, S.; Tang, Y.; Shen, M.; Zhang, G.; Shi, X. Targeted Cancer Theranostics Using Alpha Tocopheryl Succinate-Conjugated Multifunctional Dendrimer-Entrapped Gold Nanoparticles. *Biomaterials* **2014**, *35*, 7635–7646.
- (15) Tsai, Y. J.; Hu, C. C.; Chu, C. C.; Imae, T. Intrinsically Fluorescent PAMAM Dendrimer as Gene Carrier and Nanoprobe for Nucleic Acids Delivery: Bioimaging and Transfection Study. *Biomacromolecules* **2011**, *12*, 4283–4290.
- (16) Kong, L.; Alves, C. S.; Hou, W.; Qiu, J.; Mohwald, H.; Tomas, H.; Shi, X. RGD Peptide-Modified Dendrimer-Entrapped Gold Nanoparticles Enable Highly Efficient and Specific Gene Delivery to Stem Cells. *ACS Appl. Mater. Interfaces* **2015**, *7*, 4833–4843.
- (17) Xiao, T.; Hou, W.; Cao, X.; Wen, S.; Shen, M.; Shi, X. Dendrimer-Entrapped Gold Nanoparticles Modified with Folic Acid for Targeted Gene Delivery Applications. *Biomater. Sci.* **2013**, *1*, 1172–1180.
- (18) Dufès, C.; Uchegbu, L. F.; Schätzlein, A. G. Dendrimers in Gene Delivery. *Adv. Drug Delivery Rev.* **2005**, *57*, 2177–2202.
- (19) Shi, X.; Sun, Kai.; Baker, J. R. Spontaneous Formation of Functionalized Dendrimer-Stabilized Gold Nanoparticles. *J. Phys. Chem. C* **2009**, *112*, 8251–8258.
- (20) Matai, I.; Sachdev, A.; Gopinath, P. Multicomponent 5-fluorouracil loaded PAMAM Stabilized-Silver Nanocomposites Synergistically Induce Apoptosis in Human Cancer Cells. *Biomater. Sci.* **2015**, *3*, 457–468.
- (21) Naha, P. C.; Davoren, M.; Lyng, F. M.; Byrne, H. J. Reactive Oxygen Species (ROS) Induced Cytokine Production and Cytotoxicity of PAMAM Dendrimers in J774A.1 cells. *Toxicol. Appl. Pharmacol.* **2010**, *246*, 91–99.
- (22) Naha, P. C.; Byrne, H. J. Generation of Intracellular Reactive Oxygen Species and Genotoxicity Effect to Exposure of Nanosized Polyamidoamine (PAMAM) Dendrimers in PLHC-1 cells In Vitro. *Aquat. Toxicol.* **2013**, *132–133*, 61–72.
- (23) Naha, P. C.; Davoren, M.; Casey, A.; Byrne, H. J. An Ecotoxicological Study of Poly(amidoamine) Dendrimers-Toward Quantitative Structure Activity Relationships. *Environ. Sci. Technol.* **2009**, *43*, 6864–6869.
- (24) Mukherjee, S. P.; Lyng, F. M.; Garcia, A.; Davoren, M.; Byrne, H. J. Mechanistic Studies of In Vitro Cytotoxicity of Poly-(amidoamine) Dendrimers in Mammalian Cells. *Toxicol. Appl. Pharmacol.* **2010**, *248*, 259–268.
- (25) Hong, S.; Bielinska, A. U.; Mecke, A.; Keszler, B.; Beals, J. L.; Shi, X.; Balogh, L.; Orr, B. G.; Baker, J. R. Interaction of Poly(amidoamine) Dendrimers with Supported Lipid Bilayers and Cells: Hole Formation and the Relation to Transport. *Bioconjugate Chem.* **2004**, *15*, 774–782.
- (26) Mecke, A.; Majoros, I. J.; Patri, A. K.; Baker, J. R., Jr.; Banaszak Holl, M. M.; Orr, B. G. Lipid Bilayer Disruption by Polyamidoamine Dendrimers: The Role of Generation and Capping Group. *Langmuir* **2005**, *21*, 10348–10354.
- (27) Lee, H.; Larson, R. G. Lipid Bilayer Curvature and Pore Formation Induced by Charged Linear Polymers and Dendrimers: The Effect of Molecular Shape. *J. Phys. Chem. B* **2008**, *112*, 12279–12285.
- (28) Wang, W.; Xiong, W.; Wan, J. L.; Sun, X. H.; Xu, H. B.; Yang, X. L. The Decrease of PAMAM Dendrimer-Induced Cytotoxicity by PEGylation via Attenuation of Oxidative Stress. *Nanotechnology* **2009**, *20*, 105–103.
- (29) Liu, H.; Wang, H.; Xu, Y.; Guo, R.; Wen, S.; Huang, Y.; Liu, W.; Shen, M.; Zhao, J.; Zhang, G.; Shi, X. Lactobionic Acid-Modified Dendrimer-Entrapped Gold Nanoparticles for Targeted Computed Tomography Imaging of Human Hepatocellular Carcinoma. *ACS Appl. Mater. Interfaces* **2014**, *6*, 6944–6953.
- (30) Liu, H.; Wang, H.; Xu, Y.; Shen, M.; Zhao, J.; Zhang, G.; Shi, X. Synthesis of PEGylated Low Generation Dendrimer-Entrapped Gold Nanoparticles for CT Imaging Applications. *Nanoscale* **2014**, *6*, 4521–4526.
- (31) Majoros, I. J.; Keszler, B.; Woehler, S.; Bull, T.; Baker, J. R. Acetylation of Poly(amidoamine) Dendrimers. *Macromolecules* **2003**, *36*, 5526–5529.
- (32) Hu, J.; Su, Y.; Zhang, H.; Xu, T.; Cheng, Y. Design of Interior-Functionalized Fully Acetylated Dendrimers for Anticancer Drug Delivery. *Biomaterials* **2011**, *32*, 9950–9959.
- (33) Minotti, G.; Menna, P.; Salvatorelli, E.; Cairo, G.; Gianni, L. Anthracyclines: Molecular Advances and Pharmacologic Developments in Antitumor Activity and Cardiotoxicity. *Pharmacol. Rev.* **2004**, *56*, 185–229.
- (34) Torti, F. M.; Bristow, M. M.; Lum, B. L.; Carter, S. K.; Howes, A. E.; Aston, D. A.; Brown, B. W., Jr.; Hannigan, J. F., Jr.; Meyers, F. J.; Mitchell, E. P.; Billingham, M. E. Cardiotoxicity of Epirubicin and Doxorubicin: Assessment by Endomyocardial Biopsy. *Cancer Res.* **1986**, *46*, 3722–3727.
- (35) Xu, X. Y.; Ray, R.; Gu, Y. L.; Ploehn, H. J.; Gearheart, L.; Raker, K.; Scrivens, W. A. Electrophoretic Analysis and Purification of Fluorescent Single-Walled Carbon Nanotube Fragments. *J. Am. Chem. Soc.* **2004**, *126*, 12736–12737.
- (36) Sun, Y. P.; Zhou, B.; Lin, Y.; Wang, W.; Fernando, K. A. S.; Pathak, P.; Mezziani, M. J.; Harruff, B. A.; Wang, X.; Wang, H.; Luo, P. G.; Yang, H.; Kose, M. E.; Chen, B.; Veca, L. M.; Xie, S. Y. Quantum

Sized Carbon Dots for Bright and Colorful Photoluminescence. *J. Am. Chem. Soc.* **2006**, *128*, 7756–7757.

(37) Ma, Z.; Zhang, Y. L.; Wang, L.; Ming, H.; Li, H. T.; Zhang, X.; Wang, F.; Liu, Y.; Kang, Z. H.; Lee, S. T. Bioinspired Photoelectric Conversion System Based on Carbon Quantum Dot Doped Dye–Semiconductor Complex. *ACS Appl. Mater. Interfaces* **2013**, *5*, 5080–5084.

(38) Sachdev, A.; Matai, I.; Kumar, S. U.; Bhushan, B.; Dubey, P.; Gopinath, P. A Novel One-Step Synthesis of PEG Passivated Multicolour Fluorescent Carbon Dots for Potential Biolabeling Application. *RSC Adv.* **2013**, *3*, 16958–16961.

(39) Sachdev, A.; Matai, I.; Gopinath, P. Implications of Surface Passivation on Physicochemical and Bioimaging Properties of Carbon Dots. *RSC Adv.* **2014**, *4*, 20915–20921.

(40) Sachdev, A.; Matai, I.; Gopinath, P. Dual-Functional Carbon Dots–Silver@Zinc Oxide Nanocomposite: In Vitro Evaluation of Cellular Uptake and Induction of Apoptosis. *J. Mater. Chem. B* **2015**, *3*, 1217–1229.

(41) Datta, K. K. R.; Kozak, O.; Ranc, V.; Havrdová, M.; Bourlino, A. B.; Šafařová, K.; Holá, K.; Tománková, K.; Zoppellaro, G.; Otyepka, M.; Zbořil, R. Quaternized Carbon Dot-Modified Graphene Oxide for Selective Cell Labelling – Controlled Nucleus and Cytoplasm Imaging. *Chem. Commun.* **2014**, *50*, 10782–10785.

(42) Zhou, L.; Li, Z.; Liu, Z.; Ren, J.; Qu, X. Luminescent Carbon Dot-Gated Nanovehicles for pH-Triggered Intracellular Controlled Release and Imaging. *Langmuir* **2013**, *29*, 6396–6403.

(43) Zong, J.; Yang, X.; Trinch, A.; Hardin, S.; Cole, I.; Zhu, Y.; Li, C.; Muster, T.; Wei, G. Photoluminescence Enhancement of Carbon Dots by Gold Nanoparticles Conjugated via PAMAM dendrimers. *Nanoscale* **2013**, *5*, 11200–11206.

(44) Dong, W.; Zhou, S.; Dong, Y.; Wang, J.; Ge, X.; Sui, L. The Preparation of Ethylenediamine-Modified Fluorescent Carbon Dots and their use in Imaging of Cells. *Luminescence* **2015**, DOI: 10.1002/bio.2834.

(45) Liu, C.; Zhang, P.; Zhai, X.; Tian, F.; Li, W.; Yang, J.; Liu, Y.; Wang, H.; Wang, W.; Liu, W. Nano-carrier for Gene Delivery and Bioimaging based on Carbon Dots with PEI-Passivation Enhanced Fluorescence. *Biomaterials* **2012**, *33*, 3604–3613.

(46) Wang, Q.; Huang, X.; Long, Y.; Wang, X.; Zhang, H.; Zhu, R.; Liang, L.; Teng, P.; Zheng, H. Hollow Luminescent Carbon Dots for Drug Delivery. *Carbon* **2013**, *59*, 192–199.

(47) Majoros, I. J.; Myc, A.; Thomas, T.; Mehta, C. B.; Baker, J. R., Jr. PAMAM Dendrimer-based Multifunctional Conjugate for Cancer Therapy: Synthesis, Characterization, and Functionality. *Biomacromolecules* **2006**, *7*, 572–579.

(48) Li, X.; Gao, C.; Wu, Y.; Cheng, C. Y.; Xiac, W.; Zhang, Z. Combination Delivery of Adjuvant and Doxorubicin via Integrating Drug Conjugation and Nanocarrier Approaches for the Treatment of Drug-resistant Cancer Cells. *J. Mater. Chem. B* **2015**, *3*, 1556–1564.

(49) Huang, R.; Ke, W.; Liu, Y.; Jiang, C.; Pei, Y. The Use of Lactoferrin as a Ligand for Targeting the Polyamidoamine-based Gene Delivery System to the Brain. *Biomaterials* **2008**, *29*, 238–246.

(50) Tong, G.; Wang, J.; Wang, R.; Guo, X.; He, L.; Qiu, F.; Wang, G.; Zhu, B.; Zhu, X.; Liu, T. Amorphous Carbon Dots with High two-photon Fluorescence for Cellular Imaging Passivated by Hyperbranched Poly(amino amine). *J. Mater. Chem. B* **2015**, *3*, 700–706.

(51) Maiti, P. K.; Cagin, T.; Lin, S. T.; Goddard, W. A. Effect of Solvent and pH on the Structure of PAMAM Dendrimers. *Macromolecules* **2005**, *38*, 979–991.

(52) Dong, Y.; Wang, R.; Li, H.; Shao, J.; Chi, Y.; Lin, X.; Chen, G. Polyamine-Functionalized Carbon Quantum Dots for Chemical Sensing. *Carbon* **2012**, *50*, 2810–2815.

(53) Yordanov, G.; Evangelatov, A.; Skrobanska, R. Epirubicin Loaded to Pre-Polymerized Poly(butyl cyanoacrylate) Nanoparticles: Preparation and In Vitro Evaluation in Human Lung Adenocarcinoma Cells. *Colloids Surf., B* **2013**, *107*, 115–123.

(54) Sahay, G.; Alakhova, D. Y.; Kabanov, A. V. Endocytosis of Nanomedicines. *J. Controlled Release* **2010**, *145*, 182–195.

(55) Kitchens, K. M.; Foraker, A. B.; Kolhatkar, R. B.; Swaan, P. W.; Ghandehari, H. Endocytosis and Interaction of Poly (amidoamine) Dendrimers with Caco-2 cells. *Pharm. Res.* **2007**, *24*, 2138–2145.

(56) Kitchens, K. M.; Kolhatkar, R. B.; Swaan, P. W.; Ghandehari, H. Endocytosis Inhibitors prevent Poly(amidoamine) Dendrimer Internalization and Permeability across Caco-2 cells. *Mol. Pharmaceutics* **2008**, *5*, 364–369.

(57) Fornari, F. A.; Randolph, J. K.; Yalowich, J. C.; Ritke, M. K.; Gewirtz, D. A. Interference by Doxorubicin with DNA Unwinding in MCF-7 Breast Tumor Cells. *Mol. Pharmacol.* **1994**, *45*, 649–656.

(58) Olinski, R.; Gackowski, D.; Foksinski, M.; Rozalski, R.; Roszkowski, K.; Jaruga, P. Oxidative DNA damage: Assessment of the Role in Carcinogenesis, Atherosclerosis, and Acquired Immuno-deficiency Syndrome. *Free Radical Biol. Med.* **2002**, *33*, 192–200.

(59) Lo, Y. L.; Wang, W. Formononetin Potentiates Epirubicin-Induced Apoptosis via ROS Production in HeLa cells In Vitro. *Chem. Biol. Interact.* **2013**, *205*, 188–197.

(60) Riccardi, C.; Nicoletti, I. Analysis of Apoptosis by Propidium Iodide Staining and Flow Cytometry. *Nat. Protoc.* **2006**, *1*, 1458–1461.

(61) Darzynkiewicz, Z.; Bruno, S.; Del, B. G.; Gorczyca, W.; Hotz, M. A.; Lassota, P.; Traganos, F. Features of Apoptotic cells Measured by Flow Cytometry. *Cytometry* **1992**, *13*, 795–808.

(62) Rello, S.; Stockert, J. C.; Moreno, V.; Gámez, A.; Pacheco, M.; Juarranz, A.; Cañete, M.; Villanueva, A. Morphological Criteria to Distinguish Cell Death Induced by Apoptotic and Necrotic Treatments. *Apoptosis* **2005**, *10*, 201–208.

(63) Hu, D. G.; Rogers, A.; Mackenzie, P. I. Epirubicin Upregulates UDP glucuronosyltransferase 2B7 Expression in Liver Cancer cells via the p53 pathway. *Mol. Pharmacol.* **2014**, *85*, 887–897.

(64) Millour, J.; de Olano, N.; Horimoto, Y.; Monteiro, L. J.; Langer, J. K.; Aligue, R.; Hajji, N.; Lam, E. W. ATM and p53 Regulate FOXM1 Expression via E2F in Breast Cancer Epirubicin Treatment and Resistance. *Mol. Cancer Ther.* **2011**, *10*, 1046–1058.

(65) Chao, D. T.; Korsmeyer, S. J. BCL-2 family: Regulators of Cell Death. *Annu. Rev. Immunol.* **1998**, *16*, 395–419.

(66) Wolter, K. G.; Hsu, Y. T.; Smith, C. L.; Nечushtan, A.; Xi, X. G.; Youle, R. J. Movement of Bax from the Cytosol to Mitochondria During Apoptosis. *J. Cell Biol.* **1997**, *139*, 1281–1292.

(67) Liu, X.; Kim, C. N.; Yang, J.; Jemerson, R.; Wang, X. Induction of Apoptotic Program in Cell-Free Extracts: Requirement for dATP and cytochrome c. *Cell* **1996**, *86*, 147–157.

(68) Porter, A. G.; Jänicke, R. U. Emerging Roles of Caspase-3 in Apoptosis. *Cell Death Differ.* **1999**, *6*, 99–104.

(69) Lee, Y. K.; Lin, T. H.; Chang, C. F.; Lo, Y. L. Galectin-3 Silencing Inhibits Epirubicin-Induced ATP Binding Cassette Transporters and Activates the Mitochondrial Apoptosis Pathway via β -catenin/GSK-3 β Modulation in Colorectal Carcinoma. *PLoS One* **2013**, *8*, 82478.